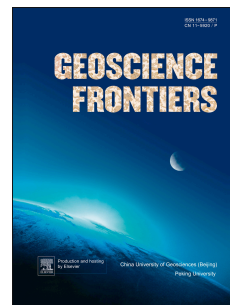


Accepted Manuscript

Highly refractory Archaean peridotite cumulates: Petrology and geochemistry of the Seqi Ultramafic Complex, SW Greenland

Kristoffer Szilas, Vincent J. van Hinsberg, Iain McDonald, Tomas Næraa, Hugh Rollinson, Jacob Adetunji, Dennis Bird



PII: S1674-9871(17)30099-3

DOI: [10.1016/j.gsf.2017.05.003](https://doi.org/10.1016/j.gsf.2017.05.003)

Reference: GSF 565

To appear in: *Geoscience Frontiers*

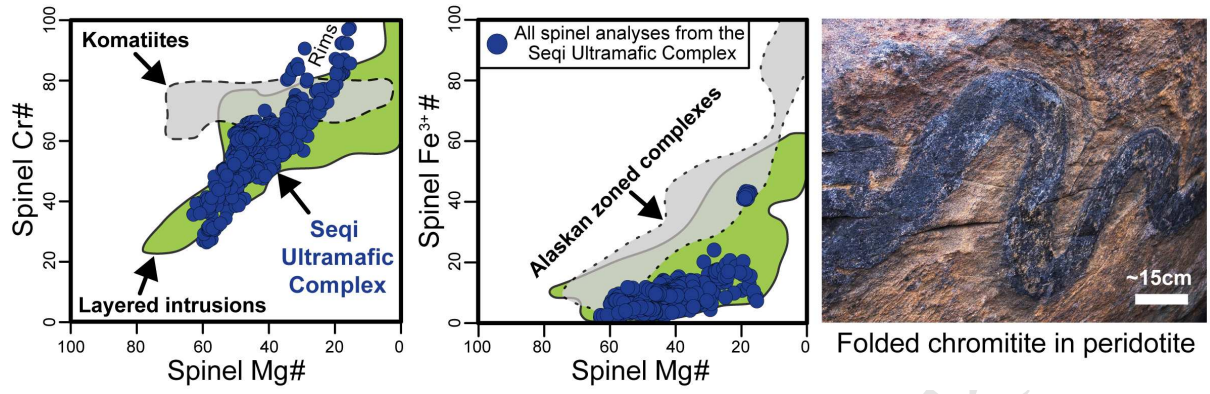
Received Date: 21 November 2016

Revised Date: 3 May 2017

Accepted Date: 21 May 2017

Please cite this article as: Szilas, K., van Hinsberg, V.J., McDonald, I., Næraa, T., Rollinson, H., Adetunji, J., Bird, D., Highly refractory Archaean peridotite cumulates: Petrology and geochemistry of the Seqi Ultramafic Complex, SW Greenland, *Geoscience Frontiers* (2017), doi: 10.1016/j.gsf.2017.05.003.

This is a PDF file of an unedited manuscript that has been accepted for publication. As a service to our customers we are providing this early version of the manuscript. The manuscript will undergo copyediting, typesetting, and review of the resulting proof before it is published in its final form. Please note that during the production process errors may be discovered which could affect the content, and all legal disclaimers that apply to the journal pertain.



ACCEPTED MANUSCRIPT

1 **Highly refractory Archaean peridotite cumulates: Petrology**
2 **and geochemistry of the Seqi Ultramafic Complex, SW**
3 **Greenland**

4
5 Kristoffer Szilas ^{a,*}, Vincent J. van Hinsberg ^b, Iain McDonald ^c, Tomas Næraa ^d, Hugh Rollinson
6 ^e, Jacob Adetunji ^e, Dennis Bird ^a

7
8 ^a Department of Geological Sciences, Stanford University, 450 Serra Mall, Stanford, CA 94305, USA

9 ^b Department of Earth & Planetary Sciences, McGill University, Quebec, Canada

10 ^c Department of Geology, Lund University, Sölvegatan 12, 223 62 Lund, Sweden

11 ^d School of Earth and Ocean Sciences, Cardiff University, Main Building, Cardiff CF10 3AT, United Kingdom

12 ^e College of Science, University of Derby, Derby, DE22 1GB, UK

13
14 * Corresponding author current address: Geological Survey of Denmark and Greenland (GEUS), Øster Voldgade 10,
15 DK-1350 Copenhagen K, Denmark

16 E-mail: kristoffer.szilas@gmail.com, szilas@stanford.edu

17 **ABSTRACT**

18 This paper investigates the petrogenesis of the Seqi Ultramafic Complex, which covers a total area
19 of approximately 0.5 km². The ultramafic rocks are hosted by tonalitic orthogneiss of the ca. 3000
20 Ma Akia terrane with crosscutting granitoid sheets providing an absolute minimum age of 2978 ± 8
21 Ma for the Seqi Ultramafic Complex. The Seqi rocks represent a broad range of olivine-dominated
22 plutonic rocks with varying modal amounts of chromite, orthopyroxene and amphibole, i.e. various

23 types of dunite (*s.s.*), peridotite (*s.l.*), as well as chromitite. The Seqi Ultramafic Complex is
24 characterised primarily by refractory dunite, with highly forsteritic olivine with core compositions
25 having Mg# ranging from about 91 to 93. The overall high modal contents, as well as the specific
26 compositions, of chromite rule out that these rocks represent a fragment of Earth's mantle. The
27 occurrence of stratiform chromitite bands in peridotite, thin chromite layers in dunite and poikilitic
28 orthopyroxene in peridotite instead supports the interpretation that the Seqi Ultramafic Complex
29 represents the remnant of a fragmented layered complex or a magma conduit, which was
30 subsequently broken up and entrained during the formation of the regional continental crust.

31 Integrating all of the characteristics of the Seqi Ultramafic Complex points to formation of these
32 highly refractory peridotites from an extremely magnesian (Mg# ~ 80), near-anhydrous magma, as
33 olivine-dominated cumulates with high modal contents of chromite. It is noted that the Seqi
34 cumulates were derived from a mantle source by extreme degrees of partial melting (>40%). This
35 mantle source could potentially represent the precursor for the sub-continental lithospheric mantle
36 (SCLM) in this region, which has previously been shown to be ultra-depleted. The Seqi Ultramafic
37 Complex, as well as similar peridotite bodies in the Fiskefjord region, may thus constitute the
38 earliest cumulates that formed during the large-scale melting event(s), which resulted in the ultra-
39 depleted cratonic keel under the North Atlantic Craton. Hence, a better understanding of such
40 Archaean ultramafic complexes may provide constraints on the geodynamic setting of Earth's first
41 continents and the corresponding SCLM.

42
43 *Keywords: North Atlantic Craton; Archaean; Dunite; Platinum-group elements; Ultra-depleted*
44 *mantle; Fiskefjord*

45

46 **1. Introduction**

47

48 Precambrian ultramafic rocks, such as komatiites, peridotites and associated cumulate rocks are of
49 economic importance for commodities including Ni, Cr and platinum-group elements (PGEs) (e.g.,
50 Naldrett, 1999; Maier, 2005; Groves and Beirlein, 2007; Begg et al., 2010). The vast majority of
51 peridotite occurrences from the Archaean and Proterozoic Eons are of cumulate rather than mantle
52 origin, and are commonly related to komatiitic lava flows, or plutonic layered intrusions and
53 anorthosite complexes, as exemplified by the localities such as the Bushveld, Fiskensæset, Mount
54 Keith, Stillwater and Windimurra complexes (Myers, 1976; Cameron, 1978; Mathison and Ahmat,
55 1996; McCallum 1996; Maier, 2005; Rosengren et al., 2005). Indisputable mantle rocks of
56 Archaean age are only known as relatively small xenoliths found in kimberlites and alkaline dykes
57 in cratonic settings (e.g., Bernstein et al., 1998; Downes, 2001; Pearson et al., 2004). The origins of
58 larger bodies of ultramafic rocks associated with Archaean greenstone belts, with postulated
59 ophiolitic affinities, are more controversial (e.g., Kusky et al., 2001; Friend et al., 2002; Rollinson,
60 2007; Zhao et al., 2007; Friend and Nutman, 2010; Szilas et al., 2015a).

61 In the North Atlantic Craton of Greenland, the greenstone/supracrustal belts are all considered to
62 be of suprasubduction zone affinity and may therefore represent ophiolitic analogues (Polat et al.,
63 2011; Furnes et al., 2015). However, in every case where associated ultramafic units were
64 investigated in detail, it was concluded that they represent olivine-dominated cumulates derived
65 from the concomitant volcanic and gabbroic sequences by fractional crystallization processes
66 (Szilas et al., 2012a, 2014c, 2015a).

67 The Mesoarchaeoan amphibolite- to granulite-facies Akia terrane of southern West Greenland
68 forms part of the North Atlantic Craton (**Fig. 1**). This terrane is dominated mainly by tonalitic

69 orthogneiss, although amphibolite and associated peridotite enclaves are found sporadically as
70 meter- to kilometre-sized inclusions throughout (Garde, 1997). The Seqi Ultramafic Complex
71 represents one such peridotite complex within the Akia terrane and this is the subject of the present
72 contribution. Its overall dimensions are approximately 500 by 1000 meters, which are distributed
73 between two main peridotite bodies and several smaller inclusions (**Fig. 2**). With the location of the
74 Seqi Ultramafic Complex at the coast, it is the most accessible of the larger peridotite occurrences
75 along Fiskefjord. Despite the fact that the Seqi Ultramafic Complex was mined for industrial grade
76 olivine from 2005–2010 by the Swedish company Minelco, there is so far only a single scientific
77 publication about the Seqi peridotites with some preliminary geochemical data (Szilas et al.,
78 2015b), and currently no accepted petrogenetic model exists for these highly refractory dunites. The
79 internal company reports that have been released mainly deal with the technical aspects of mining
80 (Christiansen, 1997, 1998; Mai, 1998; Dahl, 2004), and corresponding environmental monitoring of
81 Fiskefjord (Asmund et al., 2009; Søndergaard et al., 2009). The preliminary study of Szilas et al.
82 (2015b) proposed that the Seqi Ultramafic Complex may represent parts of a layered intrusion or
83 magma conduit that could potentially be associated with the regionally abundant mafic volcanic and
84 gabbroic rocks found throughout the Akia terrane as supracrustal belts.

85 The two main contrasting origins that can be envisioned for the Seqi peridotites, are tested
86 against the new data presented in this work: (1) residual mantle fragment that formed by large
87 degrees of melt-extraction, which left behind essentially pure dunite, as previously proposed for the
88 formation of the sub-continental lithospheric mantle (SCLM) in this region (Bernstein et al., 1998,
89 2007), or (2) alternatively the peridotites represent ultramafic cumulates formed by olivine
90 accumulation, which is also known from a range of different magma types in both extrusive
91 (komatiite vs. picrite) and intrusive (Alaskan-type vs. anhydrous layered complexes) settings (e.g.,

92 Wager et al., 1960; Irvine, 1974, 1977; Burns, 1985; McBirney, 1996; Arndt et al., 2008). The first
93 possibility would be important scientifically, because the only direct constraint on the Greenlandic
94 Archaean mantle thus far are the relatively small xenoliths derived from SCLM. If, on the other
95 hand, the Seqi peridotites formed by fractional crystallization and mineral accumulation processes,
96 this could have important economic implications given that Ni, Cr and PGE mineralization can be
97 hosted by ultramafic cumulates (Cawthorn, 1996; Zientek, 2012).

98 In the present study, a comprehensive geochemical data set is provided for dunite, peridotite and
99 chromitite from the Seqi Ultramafic Complex, which are particularly well-exposed within the Seqi
100 Olivine Mine (**Fig. 2**). Field observations and petrography are presented, in combination with bulk-
101 rock major, trace and platinum-group element data, as well as electron microprobe, LA-ICP-MS
102 and Mössbauer mineral chemistry with the aim of producing a thorough petrological and
103 geochemical characterization of the different rock types found within the Seqi Ultramafic Complex.
104 A petrogenetic model is developed based on these new data, and finally this ultramafic complex is
105 placed into a regional context with potential implications for formation the sub-continental
106 lithospheric mantle.

107

108 **2. Regional geology**

109

110 The Seqi Ultramafic Complex is located at Fiskefjord in the northern part of the Nuuk-region within
111 Mesoarchaeon tonalitic orthogneisses of the North Atlantic Craton (**Fig. 1**). It is worth noting at the
112 outset that all of the Eo- to Neoarchaeon supracrustal/greenstone belts within the North Atlantic
113 Craton of Greenland are inferred to have formed in arc-related settings (Garde, 1997, 2007; Polat et
114 al., 2002, 2007, 2011, 2015; Jenner et al., 2009; Szilas et al., 2011, 2012b, 2013a, 2017). It is

115 debatable if any other tectonic setting is represented in this region due to the consistent arc-type
116 geochemical signatures of the metabasalts (Jenner et al., 2014; Szilas et al. 2014a). Independent
117 structural observations (Bridgwater et al., 1974; Hanmer and Greene, 2002; Kisters et al., 2012;
118 Keulen et al., 2014; Polat et al., 2015) and the metamorphic evolution of the region (Dziggel et al.,
119 2014; Arai et al., 2015; Dyck et al., 2015) also support the operation of horizontal accretionary
120 processes and by inference uniformitarian plate tectonics, as being responsible for the formation of
121 the North Atlantic Craton. In further support of this interpretation is the fact that, despite several
122 decades of exploration and research, there are yet no komatiites (*s.s.*) reported from the North
123 Atlantic Craton. Thus, it is relevant to study the petrogenesis of ultramafic rocks in this region to
124 determine their origins and if they can be related to the metavolcanic rocks of the
125 supracrustal/greenstone belts, which are mostly mafic to andesitic in composition. Finally, it is
126 worth testing if any of these ultramafic rocks may represent mantle fragments.

127 The Seqi Ultramafic Complex is intruded by granitoid sheets (see field observations in **Section 3**
128 and zircon ages in **Section 5.5**), and thus it predates the ca. 3000 Ma regional continental crust-
129 forming event of the Akia terrane. Similar occurrences of large (> 100 by 1000 m) peridotite
130 enclaves and associated noritic rocks are found at the Miaggoq, Ulamertoq and Amikoq ultramafic
131 complexes marked on **Fig. 1**, and several smaller occurrences are scattered along Fiskefjord (Garde,
132 1997; Kristensen, 2006; Szilas et al. 2015b).

133 The Nuuk region consists of several discrete crustal terranes, with the oldest being the over 3600
134 Ma Itsaq gneiss complex (Nutman et al., 1996) and the youngest being the ca. 2850 Ma
135 Tasiusarsuaq terrane (Kolb et al., 2012). The majority of the crust is comprised of tonalite–
136 trondhjemite–granodiorite (TTG) suite orthogneisses, but anorthosite complexes, metavolcanic and
137 metasedimentary lithological units are also present as supracrustal/greenstone belts (Polat et al.,

138 2002; Szilas et al., 2014b, 2015a, 2016a).

139 These different terranes experienced distinct tectono-magmatic evolution, but were ultimately
140 amalgamated during the Neoarchaeon (Friend and Nutman, 2005; Nutman and Friend, 2007).
141 Peridotite bodies are also present within the Eoarchaeon Itsaq gneiss complex, but these are
142 generally not as extensive as those of the Mesoarchaeon Akia terrane; and the former appear to be
143 associated with fragmented anorthosite complexes and supracrustal belts. Thus, the peridotites of
144 the Itsaq and Akia terranes appear to be of different ages and potentially have different petrogenetic
145 origins (Bennett et al., 2002; Friend et al., 2002; Rollinson et al., 2002; Rollinson, 2007).

146 A recent overview of the igneous and metamorphic history of the Akia terrane was presented by
147 Garde et al. (2015). Some of the main geological features relevant for understanding the Fiskefjord
148 region peridotites are outlined in the following. The regional tonalite–trondhjemite–granodiorite
149 (TTG) suite orthogneisses of the Akia terrane, which host the Seqi Ultramafic Complex, have been
150 dated by U–Pb isotopes in zircon at ca. 3050–2975 Ma (Garde, 1997, 2007, 2015), although
151 subordinate dioritic gneisses with magmatic ages of about 3200 Ma are also present (Garde, 1997).
152 Supracrustal rocks (mainly tholeiitic metabasalt) form enclaves and coherent belts within the Akia
153 terrane. These metavolcanic rocks have an age of ca. 3070 Ma, based on magmatic zircon extracted
154 from volcano-sedimentary schist within the basaltic to andesitic Qussuk–Bjørneøen supracrustal
155 sequence (Garde, 2007). The Akia terrane experienced late-tectonic granulite-facies metamorphism
156 with local retrogression to amphibolite-facies at 2995–2975 Ma. Re-crystallization of zircon,
157 synkinematic intrusion of granite sheets, and isoclinal folding of the older diorites and early
158 amphibolites was associated with this event (Garde, 1997, 2007; Garde et al., 2012, 2015).

159

160 **3. Field observations and petrographical features**

161

162 Representative samples were taken in 2013 in order to characterize the different rock units that
163 comprises the Seqi Ultramafic Complex. **Fig. 3** presents key field observations from the Seqi
164 Ultramafic Complex, with additional field photos given in the supplementary **Appendix A**. The
165 latter figures are given the prefix ‘A’ when referred to in the main text.

166 The present work focuses on dunites (*s.s.*), peridotites (*s.l.*), and the chromitite of the Seqi
167 Ultramafic Complex. Amphibolite domains, reaction rims and veins are not studied in detail, as
168 these represent minor components of the Seqi Ultramafic Complex and are likely of
169 metasomatic/secondary nature, whereas the aim of the present study is to investigate the primary
170 igneous petrogenesis. As will be shown in **Section 5.3**, the oxides are generally Cr–Al-rich spinel
171 and thus, in the following discussion, spinel and chromite is used interchangeable, whereas it will
172 be specified when secondary Cr-magnetite is present. The local rock classification for Seqi of Dahl
173 (2004) is adopted here, which defines the following lithological units: homogeneous dunite, layered
174 dunite, porphyritic dunite, poikilitic dunite (here revised to peridotite), peridotite, chromitite and
175 amphibolite (**Fig. 3**). All of these rocks have been metamorphosed at upper amphibolite- to
176 granulite facies conditions and their textures are mostly granoblastic (**Fig 4**), with the exception of
177 peculiar euhedral olivine crystals found in the porphyritic dunite (**Fig. 3b**). Note that we use the
178 term ‘peridotite’ (*s.l.*) in its broadest sense to include olivine-dominated (>40%) plutonic rocks that
179 also contain various combinations of orthopyroxene and amphibole. We thus use the peridotite
180 definition of Streckeisen (1973, 1976) and Le Maitre et al. (2005) to include plutonic ultramafic
181 rocks with over 40% modal olivine with any combination of orthopyroxene and amphibole
182 regardless of origin (pyroxene–amphibole–peridotite or amphibole–harzburgite *sensu stricto*). The
183 term ‘dunite’ is used for plutonic ultramafic rocks with more than 90% modal olivine, although this

184 rock type is also a peridotite broadly speaking. For practical reasons, we thus simply distinguish
185 between different types of pure dunite (*s.s.*) versus orthopyroxene–amphibole-bearing peridotite
186 (*s.l.*) within the Seqi Ultramafic Complex.

187 Homogeneous dunite is dominated by olivine (up to 99 vol.%) and spinel typically constitutes 1–
188 3 vol.% of the rock. Retrogression of chromite to magnetite and later to chlorite is common (**Fig. 5**)
189 and this causes the rock to easily disintegrate, yielding a pure olivine sand. Metamorphic phlogopite
190 and amphibole is also present in the homogeneous dunite, but these minerals usually constitute less
191 than 1 vol.% of the homogeneous dunite unit. Dahl (2004) reported rhythmic layering and
192 crossbedding of orthopyroxene in the homogeneous dunite, which is a feature that was not observed
193 in 2013 during the fieldwork carried out for the present work, although likely the result of
194 excavation of the outcrop by mining.

195 Layered dunite is defined in the field by visible subparallel layering outlined by abundant
196 chromite in regular horizons (**Fig. 3e**). Chromite typically forms a network of interlocking
197 interstitial spinel, which gives a mesh-texture on weathered surfaces where olivine is lost (**Fig.**
198 **A13**). The chromite is also retrogressed locally to magnetite and chlorite; although not to the same
199 extent as in the homogeneous dunite. Chromite is estimated to comprise less than 5 vol.% in the
200 layered dunite, however, locally it may reach levels up to 12 vol.%.

201 Porphyritic dunite is characterized by coarse olivine with grain sizes up to about 0.5 cm and it
202 may locally contain larger (up to 3 cm) euhedral olivine crystals (**Fig. 3b**). Chromite generally has
203 as little abundance in this unit as in the homogeneous dunite with typically less than 2 vol.%.

204 Poikilitic peridotite is found only at one locality in the SE corner of the Seqi Ultramafic
205 Complex (**Fig. 2**). It consists of dunite with coarse orthopyroxene oikocrysts up to 5 cm across, that
206 readily weather out of the rock as seen in **Fig. 3f**. These orthopyroxene oikocrysts are commonly

207 single crystals that overgrow olivine, chromite and amphibole, but orthopyroxene is also present as
208 smaller grains throughout the matrix of this rock (**Fig. 4** and **Fig. 5**). Orthopyroxene comprises up
209 to 40 vol.% of this rock type and it is essentially harzburgitic.

210 Peridotite is a broadly defined unit which consists of various combinations of olivine, chromite,
211 orthopyroxene and amphibole. The mineralogical variations of the Seqi peridotites (*sensu lato*) do
212 not outline any mappable systematics, but rather reflect mixtures of these particular minerals. The
213 strict term of this unit would thus be pyroxene–amphibole–peridotite or amphibole–harzburgite, but
214 we use the term ‘peridotite’ (*s.l.*) throughout this paper to simplify the nomenclature. This unit
215 locally has a large content of green amphibole (**Fig. 3c**), which is associated with abundant
216 chromitite bands at the northern margin of the eastern enclave (**Fig. 2**).

217 Chromitite is found as cm-wide bands (up to 25 cm thick) within the peridotite unit and it is
218 usually exclusively associated with interstitial orthopyroxene and has rather sharp transitions into
219 surrounding olivine-rich domains (**Fig. 4** and **Fig. 5**). Although chromitite mainly occurs as
220 subparallel layers, it is locally strongly folded, resembling slump structures with buckling and
221 breaking of the individual bands (**Fig. 3j**).

222 Amphibolite is represented by a single sample (186463) in the present data set for the Seqi
223 Ultramafic Complex. This sample contains abundant ilmenite, which is phase that is not found in
224 any of the other studied rock units in the Seqi Ultramafic Complex. The bulk-rock and mineral
225 chemistry of the amphibolite sample is distinctly different from the rest of the studied rocks
226 (**Section 5**). This particular amphibolite sample is from an amphibole-rich domain within the
227 peridotite unit (see position in **Fig. 2**). Similar amphibole patches and veins are found throughout
228 the peridotite unit and in association with infiltrating felsic dykes and veinlets derived from the
229 granitoid host rock surrounding the Seqi Ultramafic Complex. Such amphibole veins thus appear to

230 be of secondary/metasomatic origin. Layered amphibolites and smaller lenses of hornblende are
231 also present along the western and northern margins of the main peridotite complex. Note that these
232 amphibolites have not been studied in detail, because the focus in the present work is on the various
233 types of dunite and peridotite that comprise the Seqi Ultramafic Complex. It is possible, however,
234 that the layered amphibolites may form a continuation of the olivine-dominated sequence, although
235 their contact was observed to be strongly sheared in the western part of the ultramafic complex. No
236 clinopyroxene has been observed in any of the rocks that were studied in the present work, although
237 it could be argued that any clinopyroxene would have been transformed to amphibole during the
238 metamorphic evolution of the Seqi Ultramafic Complex (see **Section 5.7**).

239 Granitoid rocks intruding the Seqi Ultramafic Complex were sampled for U–Pb zircon dating in
240 order to constrain the minimum age of the ultramafic rocks (**Section 5.5**). Sample 186451
241 represents a 20 cm wide felsic intrusive sheet with a strike of 156° and a dip of 80°W . This sheet is
242 fine grained and tonalitic in composition and it cuts the homogeneous dunite along a brittle fracture.
243 The felsic sheet has a ~ 3 cm reaction zone on either side consisting of chlorite, amphibole and talc.
244 Sample 186453 is from a 1.5 m wide NE–SW trending ($40^\circ/65^\circ\text{SE}$) pegmatite sheet that intrudes
245 the homogeneous dunite (**Fig. A5**). It has a thick (20 cm) biotite-rich reaction zone at the contact to
246 the homogeneous dunite. Sample 186456 is from the regional tonalitic orthogneiss that separates the
247 two main ultramafic blocks of the Seqi Ultramafic Complex. In the field, it is not apparent if this
248 orthogneiss has an originally intrusive or tectonic/structural contact with the Seqi Ultramafic
249 Complex. However, several dunite enclaves are present within the orthogneiss surrounding the two
250 main ultramafic bodies (**Fig. 2**), so it appears most likely that these are dismembered fragments of
251 Seqi Ultramafic Complex that were entrained in the granitoids during the formation of the regional
252 continental crust.

253

254 **4. Methods**

255

256 ***4.1 Bulk-rock major and trace element analysis***

257

258 The ultramafic samples from the Seqi Ultramafic Complex selected for bulk-rock major and trace
259 element analysis were cut into smaller pieces by diamond saw to avoid weathered surfaces. One
260 part for XRF analysis was ground in a tungsten carbide mill. Peridotites require a quartz dilution for
261 XRF, because the elevated Mg can cause crystallization in the glass bead. Therefore, a separate
262 aliquot was prepared for ICP-MS that was ground in a steel mill, which adds no contamination for
263 the elements analysed by the ICP-MS.

264 Bulk-rock major and trace element data were acquired from the geochemical laboratory at
265 Washington State University (WSU). The procedures involve flux-fusing of rock powders followed
266 by standard XRF and ICP-MS methods. Any contamination from the Li-tetraborate flux was
267 corrected for by a blank subtraction. The full analytical procedures are described on WSU's website
268 and the reader is referred to this for the method details (WSU, 2016).

269 **Table S1** in the supplementary material presents the major and trace element data, and includes
270 measurements of several international standards, as well as estimates for precision and detection
271 limits during the analysis. The XRF data have detection limits of around 20 ppm, and the ICP-MS
272 analysis accurately measured most trace elements down to around 0.5 ppm. The software GCDKit
273 of Janošek et al. (2006) was used for plotting the data. Supplementary geochemical diagrams are
274 presented in **Appendix D** and are referred to with the prefix 'D' in the following sections.

275

276 *4.2 Bulk-rock platinum-group element analysis*

277

278 Platinum-group element (PGE) and Au data were obtained at Cardiff University, UK. Rock
279 samples for PGE analysis were first cut into smaller pieces by diamond saw and the surfaces were
280 polished with sand paper to avoid any risk of metal contamination from the saw. Sample powders
281 for these analyses were milled in a ceramic shatter box to avoid metal contamination.

282 PGE and Au analysis was carried out by Ni-sulphide fire assay pre-concentration of 15 g sample
283 material, followed by Te co-precipitation and measurement by ICP-MS. A full description of the
284 instrumentation and analytical procedures are given in Huber et al. (2001) and McDonald and
285 Viljoen (2006). Accuracy for whole-rock PGE and Au was constrained by analysis of the certified
286 international reference materials SARM-64, TDB1 and WPR1, and the precision was estimated by
287 repeat analysis of a sub-set of samples. PGE data obtained on samples from the Seqi Ultramafic
288 Complex and the standards are provided in **Table S2** in the supplementary material.

289

290 *4.3. Electron microprobe mineral analysis*

291

292 Electron microprobe analysis (EMPA) of the different mineral phases was conducted at Stanford
293 University using a JEOL JXA-8230 with operating conditions of 15 kV, 20 nA, and a 2 μm spot
294 size. Counting times were 20 s on peaks and 10 s on backgrounds. Mineral standards were
295 measured at regular interval in each session to verify the accuracy of the analyses. The reader is
296 referred to the supplementary **Table S3** for the full electron microprobe data set obtained on
297 samples from the Seqi Ultramafic Complex.

298

299 **4.4. *In situ* trace element mineral analysis**

300

301 *In situ* LA-ICP-MS measurements of trace elements in minerals were conducted at McGill
302 University (Montreal, Canada) using a NewWave 213 nm Nd-YAG laser coupled to a Thermo
303 Finnigan iCAP Q ICP-MS. Material was sampled in 80 μm wide and up to 2 mm long troughs, or
304 80 μm spots for zoned minerals, at 10 Hz repetition rate and a fluence of approximately 7.5 J/cm².
305 The sample material was transported to the ICP-MS in a 800 MI/min¹ He flow, which was mixed
306 with Ar prior to injection into the plasma. The elements were split into a low-mass and a high-mass
307 set and analysed in parallel lines or adjacent spots. Mineral analyses were bracketed by NIST SRM
308 610, and reference materials BCR-2G and GSD-1G were analysed to determine accuracy. All major
309 elements were analysed in the low-mass set and data were normalised to the respective mineral
310 formulae. The high-mass data set was normalised to Mg concentrations of equivalent low-mass
311 data. **Table S4** in the supplementary material presents the *in situ* LA-ICP-MS trace element data for
312 various minerals from the Seqi Ultramafic Complex.

313

314 **4.5. Zircon U–Pb isotope data**

315

316 *In situ* LA-ICP-MS measurement of U–Pb isotopes in zircon was conducted at the Geological
317 Survey of Denmark and Greenland (GEUS). Separation of zircon was done by crushing rock
318 samples, which were then sieved at a mesh size of 300 μm . The heavy minerals were separated by
319 panning. Magnetic minerals were removed from the heavy mineral concentrate using a hand
320 magnet. Zircon grains were hand-picked from the final heavy mineral separate and were cast into
321 epoxy resin and polished to expose a central cross-section of each grain. Back scattered electron

322 (BSE) imaging was applied to reveal internal structures (**Fig. 6**), and energy dispersive
323 spectroscopy (EDS) was applied to determine inclusion chemistry. BSE and EDS were carried out
324 on a PHILIPS XL 40 SEM at GEUS.

325 The data were acquired on a Thermo Scientific Element2 magnetic mass spectrometer coupled
326 to a NewWave UP213 laser ablation system, following the procedures outlined by Gerdes and Zeh
327 (2006) and Frei and Gerdes (2009). Standard bracketing was done by analysing the Geostandard
328 zircon GJ1 (Jackson et al., 2004). Analytical sessions were started with six measurements of the
329 standard, followed by cycles of ten unknowns and three standard measurements. The laser was
330 operated with a 25 μm spot size at a repetition rate of 10 Hz with a nominal energy output of 45–
331 50% of the maximum laser intensity, corresponding to laser energy of about 0.025 mJ per pulse
332 and a laser fluence of about 3 J/cm^2 . For each analysis, the first 30 s were used to measure the gas
333 blank (background), followed by 30 s of ablation and 20 s of washout time. Helium gas was used
334 to flush the sample cell and was mixed downstream with the Ar sample gas before entering the
335 plasma of the mass spectrometer. Measured masses were: ^{202}Hg , $^{204}(\text{Pb} + \text{Hg})$, ^{206}Pb , ^{207}Pb , ^{208}Pb ,
336 ^{232}Th , ^{235}U and ^{238}U . The mass of ^{202}Hg was measured to monitor the ^{204}Hg isobaric interference on
337 ^{204}Pb .

338 Data reduction was performed using the Iolite software package (Paton et al., 2011). Data
339 processing includes: 1) baseline corrections; 2) calculating a down-hole U–Th–Pb fractionation
340 correction, and 3) applying a session-wide fractionation and instrumental drift corrections. The
341 VizualAge data reduction scheme within Iolite was used to process ‘live Concordia’ diagrams
342 (Petrus and Kamber, 2012). Isoplot 4.15 (Ludwig, 2012) was used for plotting data and for age
343 calculations. See supplementary **Table S5** for all of the U–Pb isotope data.

344

345 **4.6. Mössbauer spectroscopy of chromitite**

346

347 Mineral separates for Mössbauer spectroscopic analysis were prepared by first hammering the
348 chromitite samples into progressively smaller fragments inside plastic bags shielded by paper to
349 avoid any contamination with metal fragments from the hammer or plate. The rock grains were then
350 split by nylon mesh sieves to <500 μm and 500–700 μm size fractions, and the latter was hand-
351 picked for clean mineral separates consisting only of chromite.

352 Optical examinations of the samples show minute amounts of opaque phases (magnetite) at the
353 grain boundaries, which could be magnetically separated after crushing the sample to a fine powder
354 under acetone. Samples 186479, 186479b (replica) and 186466b have inter-grown minute crystals
355 of chromite and a non-magnetic mineral, likely orthopyroxene, which could not be separated
356 cleanly despite many repeats of hand-picking under the optical microscope.

357 ^{57}Fe Mössbauer spectroscopic measurements were made on the samples (absorbers), each
358 prepared from ~60 mg of the sample, mixed with boron nitride as a binder. The mixture was spread
359 uniformly over an area of ~1.8 cm^2 , and pressed into a pellet. The spectrometer uses a 25mCi ^{57}Co
360 in Rhodium matrix source mounted on a constant-acceleration transducer operated in a triangular
361 mode in a velocity range, ± 6 mm/s. The Doppler energies from the 14.4 keV γ -rays were detected
362 with a $\text{YAlO}_3\text{:Ce}$ scintillation counter. The data was recorded in 1024 channels, which cover twice
363 the Doppler velocity range. Spectra were calibrated with a natural α -Fe foil and all peak positions
364 reported with respect to the centroid shift (CS) of the natural α -Fe. MossA1.01a, a computer
365 program developed by Prescher et al. (2012) utilizing a full transmission integral with a normalised
366 Lorentzian source line-shape, was used to fit the Lorentzian lines of the folded data. The best fits to

367 the data were obtained by reduced χ^2 criteria. The oxidation states of Fe-ions are then characterized
368 by the centroid shift and the site occupancy determined by the quadrupole splitting (QS).

369 The uncertainties were calculated using the covariance matrix. Estimated uncertainties for CS, QS
370 and full width at half maximum (FWHM) are ± 0.020 , ± 0.030 and ± 0.025 mm/s, respectively and
371 less than $\pm 2\%$ absolute for absorption areas. A correction for the difference between the recoil-free
372 fractions at room temperature for Fe^{2+} and Fe^{3+} in the tetrahedral and octahedral sites, respectively,
373 was applied (Quintiliani, 2005). The criterion for identification of Fe-cation sites was based on the
374 relative centroid shift values, following previous reports by Pal et al. (1994), Rais et al. (2003) and
375 Rollinson et al. (2012) as $[\delta\text{Fe}^{3+}\text{A}] < [\delta\text{Fe}^{3+}\text{B}] < [\delta\text{Fe}^{2+}\text{A}] < [\delta\text{Fe}^{2+}\text{B}]$. The model was also found to
376 be appropriate in Mössbauer spectroscopic investigation of Fe-cations distribution in natural
377 chromites at different stages of oxidation (Pal et al., 1994).

378 In this study, several fitting models were tested to determine those that could be used with
379 minimum constraints. To achieve this, four models were adopted: (i) $3\text{Fe}^{2+}(\text{A}) + 1\text{Fe}^{3+}(\text{B})$ applied to
380 two samples; (ii) $2\text{Fe}^{2+}(\text{A}) + 1\text{Fe}^{3+}(\text{B})$ applied to two samples (iii) $\text{Fe}^{2+}(\text{A}) + \text{Fe}^{2+}(\text{B}) + 2\text{Fe}^{3+}(\text{B})$
381 applied to one sample. For this model, the quadrupole-splitting associated with the Fe^{2+} and Fe^{3+}
382 ions are distinguished by $[\Delta\text{qFe}^{2+}\text{B}] < [\Delta\text{qFe}^{3+}\text{B}]$. (iv) $1\text{Fe}^{2+}(\text{A}) + 2\text{Fe}^{3+}(\text{B})$ model was applied to
383 one sample. For the samples with inter-grown crystals, their $\text{Fe}^{3+}/\Sigma\text{Fe}$ ratios were only calculated
384 from the absorption areas of chromite doublets of the sample spectra. The Mössbauer data for the
385 Seqi chromitite samples are provided in **Table S6** in the supplementary material.

386

387 **5. Results**

388

389 **5.1. Bulk-rock major and trace element data**

390

391 The main bulk-rock geochemical characteristics of the different rock types in the Seqi Ultramafic
392 Complex are briefly outlined here. The Seqi rocks are comparable to the regional Fiskefjord
393 peridotites that were documented by Szilas et al. (2015b), however the Seqi dunites represent the
394 most refractory components of this suite, as seen in **Fig. 7**. Bulk-rock mg# (given as molar $\text{Mg}/[\text{Mg}$
395 $+ \Sigma\text{Fe}] \times 100\%$) assumes all iron to be divalent due to the olivine-rich nature of these rocks. Note
396 that in this work we distinguish between bulk-rock 'mg#' (which uses ΣFe) and mineral 'Mg#' (which uses Fe^{2+} only). All of the data have been recalculated on a volatile-free basis, although loss
397 on ignition (LOI) is not significant and never exceeds 1.9 wt.%.

399 The homogeneous dunite ($n = 4$), the layered dunite ($n = 3$) and the porphyritic dunite ($n = 3$) are
400 broadly similar in terms of their major element compositions (given in wt.% below) by having a
401 tight range of SiO_2 (40.3 wt.%–42.4 wt.%), MgO (45.6 wt.%–50.7 wt.%), FeOt (6.52 wt.%–8.00
402 wt.%), CaO (0.2 wt.%–0.8 wt.%), TiO_2 (0.01 wt.%–0.05 wt.%) and mg# (91.0–93.3). However, the
403 layered dunite has elevated Cr_2O_3 (1.40 wt.%–2.80 wt.%) and Al_2O_3 (1.81 wt.%–2.09 wt.%)
404 relative to the two other units (0.26 wt.%–0.58 wt.% and 0.24 wt.%–1.22 wt.%, respectively),
405 which is consistent with the larger modal chromite contents of the layered dunite.

406 The peridotite ($n = 5$) is significantly more variable in its major element composition than the
407 above-mentioned dunite and has the following ranges: 34.6 wt.% –47.1 wt.% SiO_2 , 41.3 wt.%–46.3
408 wt.% MgO , 7.76 wt.%–11.6 wt.% FeOt , 0.01 wt.%–1.98 wt.% CaO , 0.04 wt.%–0.08 wt.% TiO_2
409 and bulk-rock mg# of 87.0–90.8. Cr_2O_3 (0.93 wt.%–5.69 wt.%) and Al_2O_3 (1.60 wt.%–3.63 wt.%)
410 is also significantly more variable for the peridotites, consistent with an even greater abundance of
411 chromite than for the layered dunite. NiO correlates with MgO for all of the dunites and peridotite,
412 and ranges from 0.25 wt.% to 0.50 wt.%.

413 The poikilitic peridotite ($n = 1$) is less magnesian (MgO of 39.2 wt.% and mg# of 89.3) than the
414 above-mentioned peridotite, and more silica-rich (SiO_2 of 49.1 wt.%). This is consistent with the
415 abundant orthopyroxene in this poikilitic peridotite. It has lower NiO (0.17 wt.%) and a relatively
416 low Cr_2O_3 (0.68 wt.%) compared to the other rock types. The Seqi dunites and peridotites have a
417 $\text{CaO}/\text{Al}_2\text{O}_3$ ratio less than 0.9 and $\text{Al}_2\text{O}_3/\text{TiO}_2$ ratios ranging from 25.4 to 70.3, which is comparable
418 to those of the Fiskefjord peridotites reported by Szilas et al. (2015b).

419 The amphibolite ($n = 1$) is an outlier among the measured samples in that it has far higher TiO_2
420 (0.60 wt.%) and CaO (8.90 wt.%), in combination with low MgO (27.5 wt.%) and NiO (0.10 wt.%).
421 The mg# of the amphibolite is 83.3, whereas the remaining major elements are in the same range as
422 the other rock types from the Seqi Ultramafic Complex (**Fig. 7**).

423 Major element compositions of the chromitite samples ($n = 3$) are not plotted together with the
424 other lithological units in **Fig. 7**, because of their extreme compositions caused by their high oxide
425 contents. However, their SiO_2 contents is up to 20.1 wt.%, consistent with the presence of interstitial
426 orthopyroxene (**Fig. 4** and **Fig. 5**). Otherwise these rocks are dominated by the main components
427 constituting chromite e.g., Cr, Al, Mg, Fe and minor Ti.

428 Normative mineralogy of the Seqi rocks was calculated using a modified CIPW-norm (Kelemen
429 et al., 1992), which overall agrees with the observed modal mineralogy. The following normative
430 chromite contents was calculated: the homogeneous dunite should have between 0.3 and 0.6 mole%
431 chromite, the porphyritic dunite between 0.3 and 0.5 mole%, the poikilitic peridotite 0.8 mole%, the
432 layered dunite between 1.4 and 2.8 mole%, the peridotite between 1.0 and 5.4 mole% normative
433 chromite. The normative olivine content is calculated as: 93–96 mole% for the homogeneous
434 dunite, 93–98 mole% for the porphyritic dunite, 49 mole% for the poikilitic peridotite, 88–93
435 mole% for the layered dunite, 60–93 mole% for the peridotite. The residual normative mineralogy

436 is dominated by orthopyroxene, which is usually only predicted a few mole% for most of the Seqi
437 rocks. Two exceptions are the poikilitic peridotite, which has 47 mole% normative orthopyroxene
438 and one peridotite (186464) has 35 mole% normative orthopyroxene. These features are overall
439 consistent with what is actually observed petrographically; however, the normative calculations are
440 not able to determine the exact proportions of the minor Ca-bearing minerals that are present in the
441 Seqi rocks units. The normative calculations suggest that plagioclase, rather than amphibole (or
442 clinopyroxene) should be present, despite the fact that plagioclase is not observed in the modal
443 mineralogy of any of the studied Seqi rocks.

444 Incompatible trace element compositions of the different rock types in the Seqi Ultramafic
445 Complex appear to be controlled mainly by their modal chromite and amphibole contents (**Fig. 8**),
446 which generally yields low and high abundances, respectively. There are a few exceptions in that Ti
447 is elevated for the chromite-rich samples in addition to Pb, which is consistent with the *in situ* trace
448 element data that we present in **Section 5.4**. Because the amphibolite sample is distinct from the rest
449 of the Seqi samples and likely represents a metasomatic rock related to the intrusion of granitoid
450 sheets, we disregard this single sample in the following consideration of the bulk-rock data and
451 refer the reader to **Appendix D** for more information on this particular sample (**Fig. D3** and **Fig.**
452 **D4**). Additional geochemical plots for the rest of the samples are also presented in **Appendix D**,
453 and are referred to with the prefix 'D' in the discussion.

454 Regardless of their specific mineralogy the primitive mantle (PM)-normalised trace element
455 patterns of the Seqi rocks share several common features. They have overall U-shaped patterns with
456 elevated Th and U at up to 4 times PM values. They consistently have positive Pb–Zr–Hf anomalies
457 and mostly negative Sr–Eu-anomalies and a fairly constant Nb_{PM}/La_{PM} with a median value of 0.6.
458 All of the Seqi rocks also have U-shaped chondrite-normalised REE patterns with Gd_N/Yb_N around

459 0.5 in combination with LREE enrichment (**Fig. D2**), and generally negative Eu-anomalies.

460

461 *5.2. Bulk-rock platinum-group element data*

462

463 Platinum-group element (PGE) and Au data were determined for all of the different rock units. The
464 homogeneous dunite (n = 3) and the porphyritic dunite (n = 3) have similar PM-normalised PGE
465 patterns with the exception of one sample (186489), which has significantly lower Os and Ir
466 abundances (**Fig. 9**). The PM-normalised PGE patterns generally have smooth negative slopes with
467 distinct peaks for Au. The layered dunite samples (n = 3) all have a distinct trough at Os and Ir, but
468 are otherwise mostly within the range of abundances as the other types of dunite. The poikilitic
469 peridotite (n = 1) has flat PM-normalised pattern and PGE abundances similar to that of PM,
470 although it also has a small positive Au-anomaly, caused by lower Pd and Cu abundances than for
471 PM. The peridotite samples (n = 3) have similar PGE patterns as the homogeneous and porphyritic
472 dunites, including the positive Au-anomalies. The chromitite (n = 7) is the most PGE-rich rock
473 types at the Seqi Ultramafic Complex with ranges (in ppb) of Os from 2.12 to 29.3, Ir from 2.14 to
474 24.2, Ru from 9.31 to 60.3, Rh from 1.59 to 7.4, Pt from 7.96 to 156.3, and Pd from 5.90 to 92.5.
475 Interestingly, the metasomatic amphibolite sample (186463) has even higher Os (45.7 ppb) and Ir
476 (39.0 ppb) abundances than the chromitites (**Fig. D5**). The amphibolite has a total Σ PGE content of
477 178 ppb, whereas the highest Σ PGE for chromitite is 181 ppb. There is an apparent negative
478 correlation for the Seqi rocks between their bulk-rock mg# and Ir (and Os) abundances (**Fig. D7**),
479 which suggests that olivine was not the primary host of the PGEs.

480

481 *5.3. Electron microprobe mineral data*

482

483 Olivine is highly forsteritic (olivine Mg# given as molar $\text{Mg}/[\text{Mg} + \text{Fe}^{2+}] \times 100$) in all of the Seqi
484 rock units with the following compositional Mg# ranges: 90.9–95.3 for chromitite, 91.6–93.3 for
485 homogeneous dunite, 91.8–94.6 for layered dunite, 90.8–92.0 for peridotite, 92.0–93.7 for
486 porphyritic dunite and 93.1–93.5 for euhedral crystals in the porphyritic dunite (**Fig. 10**). Olivine is
487 essentially unzoned in all the Seqi rocks and only displays slight enrichment in Mg# at the rims
488 where grains are in contact with chromite (**Fig. D19**). This disturbance of Mg# is particularly
489 pronounced for the chromitites (**Fig. 10**), where olivine grains extend to the highest Mg# recorded
490 among all of the Seqi rock types, which is consistent with subsolidus Fe–Mg exchange between
491 spinel and olivine.

492 As seen in **Fig. 10**, the olivine compositions of the layered dunite and the homogeneous dunite
493 have an apparent bimodal forsterite distribution (Mg# of around 92.0 vs. 93.2). However, this
494 feature is generally uncorrelated with the bulk-rock mg# of the measured samples, which is mainly
495 determined by the modal spinel contents of the rocks (**Fig. 11a**). This effect is obvious for the
496 peridotites, which have the lowest overall forsterite contents, and yet their bulk-rock mg# displays
497 the largest range of the Seqi rocks, which suggests that olivine Mg# is independent of the chromite
498 contents.

499 NiO in olivine does not show any systematic variation among the different lithological units,
500 which have the following ranges: 0.33 wt.%–0.61 wt.% for chromitite, 0.30 wt.%–0.53 wt.% for
501 homogeneous dunite, 0.35 wt.%–0.51 wt.% for layered dunite, 0.33 wt.%–0.56 wt.% for peridotite,
502 0.26 wt.%–0.58 wt.% for porphyritic dunite and the euhedral crystals in the porphyritic dunite have
503 a range of 0.32 wt.%–0.51 wt.%. The median NiO contents of the Seqi olivine is 0.44 wt.% (**Fig.**
504 **D8**).

505 Oxides in the different rock units of the Seqi Ultramafic Complex are generally Cr-rich spinel,
506 hereafter simply referred to as chromite or spinel interchangeably. The spinel data were filtered by
507 excluding analyses with significant Si+Na (>0.006 cpfu), given that these two elements are
508 incompatible in the spinel structure and therefore likely reflect inclusion-rich grains. Chromite with
509 >0.5 cpfu Fe (and $\text{Fe}^{3+\#} > 15$) is assumed to represent grains that were affected by metamorphic re-
510 equilibration, which is supported by their general enrichment in Mn and Ti, in combination with
511 low Mg content (**Fig. D13**). These characteristics are typical of metamorphosed chromite and can
512 be used to discriminate such grains from primary igneous spinel compositions (Hattori and Guillot,
513 2007; Bernstein et al., 2013; Colás et al., 2014). Spinel in the Seqi rocks is generally unzoned, but
514 do display elevated Cr# and low Mg# at rims in contact with olivine. This is also the case when
515 spinel is being replaced by chlorite. There is clear evidence of secondary processes affecting the
516 chromite rims to yield Cr-rich magnetite, which is also associated with an increase in TiO_2 by
517 residual enrichment (**Fig. D13**). An example of this reaction is seen in **Fig. 5**, where the ‘spongy’
518 texture of the spinel in the homogeneous dunite, is caused by replacement of chromite with chlorite,
519 resulting in Fe–Ti–Mn-enrichment in the residual chromite to the point that it becomes Fe-rich
520 chromite with essentially no Mg or Al, which are taken up by the newly formed chlorite.

521 The spinel Cr# (calculated as molar $\text{Cr}/[\text{Cr} + \text{Al}] \times 100$) ranges from 26.4 to 97.4 for the various
522 types of dunite and peridotite, but forms a much tighter range from 55.7 to 70.1 for the chromitite.
523 The same is observed for spinel Mg#, which ranges from 15.4 to 62.9 for the dunite and peridotite
524 and from 33.7 to 50.5 for the chromitite (**Fig. 12**). Spinel $\text{Fe}^{3+\#}$ is calculated assuming
525 stoichiometry (given by molar $\text{Fe}^{3+}/[\text{Fe}^{3+} + \text{Al} + \text{Cr}] \times 100$) and generally falls below about 20, with
526 the exception of the anomalous amphibolite sample (186463), which plots at just over 40. This
527 sample also contains abundant ilmenite (**Fig. D9**).

528 All of the pyroxenes that were measured are nearly pure enstatite orthopyroxene, regardless of
529 their lithological host and form a tight range of compositions from $\text{En}_{89.4}$ to $\text{En}_{92.4}$, $\text{Fs}_{7.19}$ to $\text{Fs}_{10.4}$,
530 and $\text{Wo}_{0.07}$ to $\text{Wo}_{0.09}$ (**Fig. 11b**). TiO_2 is less than 1.1 wt.%, Al_2O_3 is less than 2.6 wt.% and the
531 median Cr_2O_3 contents is 0.21 wt.%. Their Mg# ranges from 89.4 to 92.6 (median of 91.0).

532 Amphibole is present mainly in the peridotite and the amphibolite units of the Seqi Ultramafic
533 Complex, although minor amounts are also found in some of the different types of dunites. Two
534 types of amphibole are found: (1) tremolite is mainly present in the amphibolite unit and as
535 inclusions within euhedral olivine crystals of the porphyritic dunite, (2) magnesio-hornblende is
536 present in the peridotite, as well as a minor phase in the various dunites. The attribution scheme of
537 Hawthorne et al. (2012) was used to calculate the amphibole compositions and to estimate the
538 $\text{Fe}^{3+}/\text{Fe}^{2+}$ ratio.

539 Tremolite Mg# (in the C-site) ranges from 96.2 to 100. SiO_2 ranges from 47.1 wt.% to 55.7 wt.%
540 (Si of 7.24 to 7.99 cpfu). TiO_2 is less than 0.8 wt.% ($\text{Ti} < 0.07$ cpfu), Cr_2O_3 is less than 1.8 wt.%
541 ($\text{Cr} < 0.13$ cpfu), Fe^{3+} is less than 0.25 cpfu, Fe^{2+} is less than 0.19 cpfu, while MgO is up to 23.5
542 wt.% (Mg < 4.85 cpfu at the C-site). Magnesio-hornblende Mg# (in the C-site) ranges from 95.5 to
543 99.9. SiO_2 ranges from 48.6 wt.% to 58.2 wt.% (Si from 6.74 to 7.44 cpfu). TiO_2 is less than 0.7
544 wt.% ($\text{Ti} < 0.09$ cpfu), Cr_2O_3 is less than 1.4 wt.% ($\text{Cr} < 0.20$ cpfu), Fe^{3+} is less than 0.42 cpfu, Fe^{2+} is
545 less than 0.21 cpfu, while MgO is up to 23.8 wt.% (Mg < 4.52 cpfu at the C-site).

546 Amphibole is interpreted to be metamorphic in origin, and to represent replacement of primary
547 igneous pyroxene. In **Fig. 11b**, amphibole compositions have been recalculated on a volatile free
548 basis and converted to the corresponding pyroxene stoichiometry. As can be seen in **Fig. 11b**, the
549 corresponding pyroxene composition would range in from $\text{En}_{62.5}$ to $\text{En}_{70.5}$, $\text{Fs}_{2.08}$ to $\text{Fs}_{8.10}$, and
550 $\text{Wo}_{27.0}$ to $\text{Wo}_{29.8}$, and would thus be clinopyroxene (augite). However, we note that if orthopyroxene

551 has participated in the reaction of clinopyroxene to form metamorphic amphibole, it would not
552 allow for the clinopyroxene composition to be reconstructed per the above recalculation. A
553 clinopyroxene precursor origin for amphibole is supported by the *in situ* LA-ICP-MS mineral data
554 presented in the following section that show negative Ta–Nb–Ti-anomalies (**Fig. 13**). Further
555 evidence for the presence of igneous clinopyroxene is the elevated Ti content in some spinel rims,
556 which has been interpreted to represent metamorphic re-equilibration and redistribution of Ti.
557 Clinopyroxene can contain significant Ti in ultramafic igneous rocks and is a potential source of
558 this Ti enrichment in spinel. Given that Ti mobility in aqueous fluids is low, this argues against a
559 metasomatic introduction. Residual enrichment of Ti (and Fe + Mn) in spinel has also been
560 observed, but only where chlorite replaces spinel, which represents a much later retrogression (see
561 above and **Fig. 5** and **Fig. D13**).

562

563 **5.4. *In situ* LA-ICP-MS mineral data**

564

565 The trace element contents of the main rock-forming minerals (olivine, chromite, orthopyroxene
566 and amphibole) in the Seqi Ultramafic Complex were measured *in situ* by LA-ICP-MS. Olivine has
567 low levels of incompatible trace elements with the exception of large positive anomalies for Pb at
568 up to 3 times primitive mantle abundances (**Fig. 13**). Chromium, Al, V and, to a lesser extent, Zn
569 concentrations are affected by small spinel inclusions in the olivine, and the true concentrations in
570 olivine appear to be a factor of 10 lower for Al, Cr and V, and a factor of 2 lower for Zn.

571 Spinel is the second-most depleted mineral. Besides enrichment in Pb, chromite has large
572 positive anomalies for Ti. Orthopyroxene has a relatively smooth U-shaped trace element pattern
573 with distinct positive anomalies for Th–U–Pb–Ti. Amphibole is the most incompatible trace

574 element-rich mineral, and generally has negative anomalies for the high field strength elements
575 (HFSEs). Phlogopite is enriched in large ion lithophile elements (LILEs) in addition to Nb–Ta–Ti,
576 but this mineral is not present in modal abundances that would make it critical in bulk-rock
577 reconstruction of any of the rock types at the Seqi Ultramafic Complex. Furthermore, it likely
578 represents a metasomatic product related to the fluid infiltration from the intruding granitoid host
579 rocks.

580

581 *5.5. Zircon U–Pb isotope ages*

582

583 Sample 186456 (tonalitic orthogneiss) has zircon grains that are mainly prismatic with aspect ratios
584 around 2 to 4 and lengths of 200–300 μm . Zircon grains contain a variety of internal textural
585 domains, with both growth zoned or homogeneous cores and inclusion rich rim domains. **Fig. 6a**
586 shows examples of the different domains, where preserved growth zoning is observed in grains a1
587 and a2. In grain a3 the core domain appears homogeneous and one end of the grain is strongly
588 disturbed and inclusion rich. In grains a4 and a5 disturbed domains are observed as back-scattered
589 electron (BSE) dark regions, however remaining original zoning patterns are also observed. Zircon
590 U–Pb isotope analyses have mainly been focused on core domains, with few spots placed in rim
591 domains in this sample. The disturbed rim domains are relatively rich in common-Pb and analyses
592 with low $^{206}\text{Pb}/^{204}\text{Pb}$ have been corrected for common-Pb. The data are mainly concordant and
593 except for four analyses the remaining 39 spots are within $\pm 10\%$ of discordance. Th/U values
594 mainly range from 0.1 to 0.5 with the lowest values corresponding to some of the lowest ages,
595 however they do not display any obvious trends. $^{207}\text{Pb}/^{206}\text{Pb}$ ages range from 2749 to 2997 Ma and
596 by choosing analyses in core domains with least textural evidence for disturbance, an average

597 $^{207}\text{Pb}/^{206}\text{Pb}$ age of 2977 ± 7 Ma ($n = 15$; $\text{MSWD} = 0.67$) is obtained for this sample. Using the same
598 data an intercept age of 2978 ± 8 Ma is obtained (**Fig. 14a**), and this age is interpreted to represent
599 the intrusive age of the orthogneiss protolith.

600 Sample 186451 (tonalite sheet) has zircon grains that are large (mainly $> 300 \mu\text{m}$) and stubby
601 with aspect ratios from 1 to 3. Internal textures are mainly homogeneous, many grains have rather
602 wide zones that are parallel to the crystal faces (**Fig. 6b**). Some grains have narrow rims or partial
603 rims with irregular boundaries toward the core of the grains and low BSE intensity (**Fig. 6b**, grains
604 b2, b3). Trails of inclusions are present in many grains and they commonly occur in two to three
605 orientations (**Fig. 6b**, b1, b3). Zircon grains from this sample are relatively poor in U (mean of 50
606 ppm) and the ^{204}Pb signal is mainly at background levels. Analyses are concordant and plot in a
607 rather narrow group (**Fig. 14b**). The average of all analyses (rejecting outliers on a 2σ level) yield
608 an age of 2969 ± 5 Ma ($n = 41/45$; $\text{MSWD} = 0.92$). This age is interpreted to reflect the
609 crystallization age of the tonalitic sheet, which is indistinguishable from sample 186456 within the
610 error of the analyses.

611 Sample 186453 (pegmatite) has zircon grains that are prismatic. The grains have a large variation
612 in sizes from 100 to 700 μm , with the larger grains being more abundant. These grains have a
613 brownish colour. Internal textures are divided into two main domains; internal core regions, which
614 are mostly either homogeneous or growth zoned and BSE bright regions which are, often rims
615 domains (**Fig. 6c**). The BSE bright domains are commonly inclusion rich (**Fig. 6c**, grain c2) and
616 contain irregular low intensity BSE regions (**Fig. 6c**, c1). Zircon U–Pb isotope analyses have
617 mainly been focused on core domains. There is a high common Pb contents in many of the
618 analyses, and overall a positive correlation between $^{206}\text{Pb}/^{204}\text{Pb}$ and $^{207}\text{Pb}/^{206}\text{Pb}$ age is observed.
619 Common-Pb is mainly present in BSE bright rim domains, but also in some texturally undisturbed

620 core regions. Analyses are generally concordant, and plot in one coherent group (**Fig. 14c**), which
621 range in age from 3014 to 2816 Ma. There is no observable correlation between Th/U and
622 $^{207}\text{Pb}/^{206}\text{Pb}$ age. By selecting analyses from unaltered core domains an average $^{207}\text{Pb}/^{206}\text{Pb}$ age of
623 2940 ± 5 Ma ($n = 59/65$; MSWD = 1.4) is obtained, which is interpreted as the crystallization age of
624 the pegmatite. Analyses from BSE bright rim domains yield a $^{207}\text{Pb}/^{206}\text{Pb}$ age 2915 ± 10 Ma ($n =$
625 $20/21$; MSWD = 1.2), which suggest that Pb-loss affected these regions; however, this age might
626 not have any geological meaning.

627

628 **5.6. Mössbauer spectroscopy data**

629

630 Mineral separates from five chromitite samples were analysed by the Mössbauer method at Derby
631 University using the procedure described by Rollinson et al. (2012). The following $\text{Fe}^{3+}/\Sigma\text{Fe}$ ratios
632 were determined: 0.157, 0.184, 0.192, 0.209 and 0.470. In **Fig. 15**, we present two of the obtained
633 spectra as examples of models (i) and (iii), respectively (see **Section 4.6**). The remaining spectra, as
634 well as the data, are given within **Table S6**. A single sample (186469) has elevated $\text{Fe}^{3+}/\Sigma\text{Fe}$ of
635 0.470, and it also has relatively low PGE contents (**Section 5.2**) and low SiO_2 (4.50 wt.%), but is
636 otherwise similar to the rest of the chromitite samples. However, this sample has the largest range in
637 spinel $\text{Fe}^{3+}\#$ from 8 to 15, elevated spinel Mg# of about 50, and it is the most chlorite-rich of the
638 chromitite samples. Therefore, it appears that this particular sample was affected by metamorphic
639 retrogression, which resulted in formation of Cr-rich magnetite, as well as chlorite at the expense of
640 igneous chromite (**Fig. 5**). All the results of the $\text{Fe}^{3+}/\Sigma\text{Fe}$ obtained from Mössbauer analyses are
641 plotted in **Fig. 16**, along with estimates based on EMPA and LA-ICP-MS measurements of spinel
642 calculated by assuming stoichiometry.

643

644 *5.7. P–T constraints and metamorphic history*

645

646 The igneous paragenesis of the Seqi Ultramafic Complex is dominated by olivine, chromite,
647 orthopyroxene, and variable clinopyroxene (which is now present as amphibole, see **Section 6.2**).
648 There is no petrographical, nor geochemical evidence for garnet having been present in these rocks,
649 which constrains the upper pressure of emplacement to ~2.4 GPa, below which spinel is the
650 aluminous phase. The olivine–spinel Al-exchange thermometer of Wan et al. (2008), when applied
651 to spinel core compositions and the 3rd quartile Al content of associated olivine cores, provides
652 temperature estimates between 1200 and 1250°C. Olivine–spinel rims in direct contact give Al-
653 temperatures that are 50°C lower, indicating some, but minor, re-equilibration of Al-contents during
654 subsequent metamorphism. The 1200–1250°C temperature is close to the dry peridotite solidus and
655 indicates that the parental melt had an activity of H₂O of <0.15 at high pressure or essentially dry at
656 the low end of the pressure range.

657 Preservation of magmatic structures and textures in chromite and olivine on outcrop and thin
658 section scales indicates limited metamorphic mineral replacement despite granoblastic textures, and
659 minimal hydration, in agreement with overall dry conditions. Minor tremolite inclusions suggest
660 initial cooling to below ~680°C, but the peak metamorphic stage does not contain amphibole,
661 except in samples that we interpret as not preserving their magmatic compositions. Peak
662 metamorphic assemblages for the various Seqi rocks are olivine + spinel, olivine + spinel +
663 orthopyroxene, and olivine + spinel + orthopyroxene + phlogopite. Clinopyroxene would also have
664 been stable at this stage if its presence is accepted.

665 *P–T* conditions for this peak metamorphic stage were constrained by constructing pseudosections

666 using PerpleX (Connolly, 2005), using the thermodynamic database of the Holland and Powell
667 (2011) and associated solution models for amphibole, olivine, pyroxene, Cr-spinel, serpentine, talc,
668 garnet, biotite and plagioclase (Jennings and Holland, 2015; Diener and Powell, 2012). The
669 presence of phlogopite as the sole K-bearing and hydrous phase in sample 186489 limits the water
670 content to between 0.05 and 0.15 wt.%, and a common value of 0.1 wt.% was used in all
671 calculations. Also note that Cr was included in the pseudosection calculations to account for the
672 effect that it has on increasing the spinel stability range. **Fig. 17** shows the fields where the sample
673 paragenesis is predicted to be stable for each sample. These fields overlap to constrain conditions
674 from 700 to 900°C at 1.0 to 2.3 GPa, bordered by the lack of garnet (maximum P), clinopyroxene
675 (maximum T), plagioclase (minimum P) and various hydrous phases (minimum T). If
676 clinopyroxene was present at this stage, the pressures and temperatures could potentially have been
677 higher (dashed field in **Fig. 16**)

678 A variety of geothermometers was applied to mineral rim compositions and contact mineral pairs
679 (**Fig. 17** inset). Mg–Fe exchange thermometers underestimate temperatures, likely owing to low
680 blocking temperatures for Mg–Fe inter-diffusion, whereas olivine–orthopyroxene Ni-exchange may
681 suffer from incomplete metamorphic equilibration. Ca-solubility thermometry should strictly be
682 regarded as minimum temperature estimates, because the Ca-saturating phase clinopyroxene is
683 missing, but we interpret this to be an absence related to retrogression consistent with regional
684 interpretations (Garde, 1997). The geothermometers converge to the lower temperature half of the
685 pseudosection field.

686 Peak metamorphism was followed by several retrogression episodes, producing varying amounts
687 of amphibole, serpentine and talc, followed by chlorite, and leading to retrogression of chromite to
688 Cr-magnetite and further to chlorite. This retrogression is accompanied by hydration, and may have

689 been instigated by granitoid intrusion given the similarity in mineral phases in the granitoid-
690 ultramafic reaction rims.

691

692 **6. Discussion**

693

694 A large ultramafic rock body like that of the Seqi Ultramafic Complex could either represent a
695 mantle fragment or olivine-rich cumulates derived by fractional crystallization processes in the
696 crust. In the latter case one would need to distinguish between: (1) komatiite-related dunite formed
697 by inflation of a lava flow channel (Arndt et al., 2008), (2) a layered intrusive complex formed by *in*
698 *situ* crystal fractionation, as exemplified by world-class localities like the Bushveld, Muskox,
699 Skaergaard and Stillwater complexes (Irvine, 1977; McBirney and Noyes, 1979; McCallum et al.,
700 1980; Eales and Cawthorn, 1996; Spandler et al., 2005; Nielsen et al., 2015), or (3) alternatively a
701 zoned Ural-Alaskan type ultramafic complex, which represents arc-related magma conduits (Irvine,
702 1974; Burns, 1985; DeBari and Coleman, 1989). In the following discussion, these different
703 hypotheses are evaluated by employing a holistic approach to the new bulk-rock and mineral
704 geochemical data presented in the previous sections.

705

706 **6.1. Bulk-rock geochemical features**

707

708 Mantle rocks represented by dunite should either have formed as highly depleted residues that
709 experienced large degrees of melt extraction or alternatively they could be the products of melt-rock
710 interaction (e.g., Kelemen et al., 1992; Bernstein et al., 1998). Cumulate dunite formed in the crust
711 on the other hand forms by olivine segregation from a magnesian magma, and it would be

712 mineralogically similar, but petrographically distinct. However, the Seqi Ultramafic Complex has
713 experienced granulite- to upper amphibolite-facies metamorphism, which is consistent with the
714 persistent granoblastic textures (**Fig. 4** and **Fig. 5**), and thus the petrographical features are difficult
715 to directly apply to this distinction.

716 Both mantle rocks and peridotite cumulate rocks formed within the crust should theoretically
717 have extremely low trace element abundances due to the loss of these components and lack of
718 incorporation in fractionating olivine, respectively. It should be noted that all of the Seqi
719 peridotites (*s.l.*, including the dunites) have elevated Th contents, whereas abyssal, ophiolitic and
720 orogenic peridotites commonly have negative Th-anomalies (Bodinier and Godard, 2003; Niu,
721 2004). Despite this obvious difference, the overall trace element abundances of the Seqi rocks are
722 nonetheless similar to those of mantle rocks (**Fig. D21**). Recently, however, it has become clear that
723 the incompatible trace element contents of mantle residues are far more enriched than can be
724 accounted for by melt extraction models (Warren, 2016). This means that trace element abundances
725 are controlled to a higher degree by melt-rock reaction than by pure melt depletion, and thus trace
726 element patterns are hardly a diagnostic feature of mantle rocks.

727 When comparing the major element compositions of abyssal peridotites with those of the Seqi
728 rocks (**Fig. D20**), it is noted that the latter extend to far higher MgO, Ni and Cr and have lower CaO
729 and SiO₂ contents. The chromite compositions of the Seqi rocks also argue against them
730 representing mantle rocks (**Fig. 12**), as will be discussed further in **Section 6.2**.

731 The Seqi bulk-rock compositions show better geochemical overlap with olivine-rich cumulates
732 associated with komatiites (**Fig. D27**). However, the Al₂O₃/TiO₂ ratios of the Seqi rocks are around
733 40, which is significantly different from that of the two main types of komatiite (Barberton-type ~
734 15 and Munro-type ~ 19). The peridotites (MgO>20 wt.%) of the Fiskefjord region have an average

735 value of around 42, which agrees with the Seqi rocks and clearly distinguishes them from komatiitic
736 cumulates (**Fig. 18**). The $\text{CaO}/\text{Al}_2\text{O}_3$ ratios of the Seqi rocks are generally low (<0.44). The Al_2O_3
737 contents of the Seqi rocks is controlled by the modal contents of chromite, which is generally high
738 in comparison to komatiitic cumulates, as also seen by the elevated Cr of the Seqi rocks (**Fig. 18**).
739 Additionally, the moderately incompatible trace element abundances of the Seqi rocks (including
740 TiO_2) are relatively low, giving them U-shaped patterns, which is evident from a significantly lower
741 $\text{Gd}_\text{N}/\text{Yb}_\text{N}$ ratio than for komatiitic cumulates (**Fig. 18**).

742 The PGE patterns of the various Seqi dunites display either a relatively smooth negative pattern
743 at around 1 to 0.1 times PM or an IPGE-depleted pattern (**Fig. 9**). None of these patterns resemble
744 those of dunite channels in the Oman mantle section, which have scattered patterns due to local
745 sulfide dissolution by percolating melts (Hanghøj et al., 2010). Strong negative IPGE (iridium-
746 affinity PGEs) fractionation is a typical feature of magmas and their derivative cumulates, whereas
747 mantle rocks generally have flat PM-normalised PGE patterns (Hattori and Hart, 1997; Hattori and
748 Shirahase, 1997; Hattori and Guillot, 2007). IPGE fractionation in primitive magmas occur when
749 the degree of mantle melting was not high enough to completely deplete the source of sulfide or
750 alternatively if the primary melt that had previously fractionated Os–Ir-alloys in the magma conduit
751 (Barnes and Fiorentini, 2008; Fiorentini et al., 2011; Gannoun et al., 2016). In contrast, mantle
752 residues usually display systematic PPGE fractionation depending on their degree of melt depletion
753 (e.g., Pearson et al., 2004; Luguet et al., 2007; Maier et al., 2012).

754 Clearly the Seqi dunites with bulk-rock MgO in excess of 45 wt.% are not primary magmas, and
755 thus the IPGE-depleted dunites likely represent cumulates formed at a late stage where IPGE-alloys
756 had already precipitated. The apparent negative correlation between bulk-rock mg# and Ir (and Os)
757 abundances suggest that IPGE-rich alloys did not saturate until after the earliest formed olivine

758 (**Fig. D7**). Bulk-rock mg# is clearly controlled by the addition of cumulus chromite (**Fig. 11**), and
759 there is also a strong positive correlation between IPGE contents and the chromite abundance of the
760 different Seqi samples (**Fig. D7**). This is especially obvious if also considering the chromitite
761 samples. This affinity of certain PGEs for chromite is a common feature of fractional crystallization
762 that is observed in a range of different magma types (Ballhaus, 1998; Pagé and Barnes, 2016).

763 Komatiites tend to have slightly positive slopes on a PM-normalised PGE diagrams due to the
764 more incompatible nature of the PPGEs (platinum-affinity PGES) than the IPGEs, however their
765 derivative cumulates have essentially flat patterns (Fiorentini et al., 2011). This is unlike the Seqi
766 rocks, which have slightly negative slopes and thus low Pd/Ru ratios and lower Cu abundances than
767 komatiites and their associated cumulates. It should be noted that the positive Au-anomaly is a
768 feature that is also observed for komatiite cumulates, however, overall the vastly different Ni/Cu,
769 Al_2O_3/TiO_2 in combination with the U-shaped trace element patterns (elevated Th and lower
770 Gd_N/Yb_N ratios), suggest that the Seqi Ultramafic Complex was not derived from a komatiitic
771 primary magma. However, we note that plutonic ultramafic rocks (dunite) associated with
772 Phanerozoic komatiites on Gorgona Island in the Caribbean have been interpreted by Révillon et al.
773 (2000) to represent the plumbing system (magma conduit) of an oceanic plateau. A similar
774 interpretation of the Seqi Ultramafic Complex appears feasible as we will point out in **Section 6.3**
775 below.

776

777 ***6.2. Mineral compositional fingerprints***

778

779 Although it is possible that the Seqi peridotites experienced serpentinisation at some point (e.g.,
780 during early crustal accretion) and later prograde olivine growth during granulite-facies

781 metamorphism, there are a number of arguments against this: 1) the preservation of apparent
782 primary igneous layering and slump textures in chromitite; 2) the high Al-content of olivine cores,
783 which preserves magmatic temperatures (**Section 5.7**); and 3) the low $a_{\text{H}_2\text{O}}$ conditions constrained
784 by peak metamorphism would be incompatible with prograde metamorphism from a completely
785 hydrated protolith.

786 Mg–Fe exchange thermometers do document redistribution of Mg and Fe during metamorphism
787 among spinel, olivine and orthopyroxene, but given the dry conditions, this is interpreted to largely
788 take place under closed system conditions and be confined to mineral rims and smaller grains. The
789 temperatures that are recorded by spinel–olivine Fe–Mg exchange and by Al–Cr in orthopyroxene
790 are not consistent as explained in **Section 5.7**. The latter system records temperatures that
791 correspond well with the observed mineralogy with an assemblage of olivine + orthopyroxene +
792 tremolite in the peridotites, which would place the metamorphic conditions of these rocks at a
793 temperature above 700°C.

794 As mentioned previously, calculated bulk-rock mg# of the Seqi rocks is controlled by the modal
795 amount of chromite (**Fig. 11a**). The left-ward displacement from the 1:1 ratio in **Fig. 11a** to lower
796 than expected bulk-rock mg# is directly proportional to the normative chromite contents of the
797 rocks, with the homogeneous and porphyritic dunites having less than 0.6 mole% chromite, the
798 layered dunites having between 1.4 and 2.8 mole% chromite, and the peridotites having between 1.0
799 to 5.4 mole% normative chromite (**Section 5.1**). This is further evidence that there has been
800 minimal subsolidus re-equilibration between olivine and spinel and that the olivine cores reflects
801 the Mg/Fe ratio of the melt from which they crystallized, regardless of the amount of trapped
802 chromite in these olivine-dominated cumulates. It seems reasonable to assume that the olivine-
803 dominated Seqi rocks preserve their primary igneous olivine compositions with local subsolidus

804 exchange with chromite being limited to spinel rims (**Fig. D19**).

805 The well-established relationship between Fe–Mg exchange of melt and liquid (Roeder and
806 Emslie, 1970), suggest that the most abundant lithological units of the Seqi Ultramafic Complex
807 (layered dunite and homogeneous dunite) with a maximum forsterite content of 93.2, were derived
808 as cumulates from a melt with the liquid-Mg# up to 80.

809 The relationship between melt and chromite compositions of Maurel and Maurel (1982), which
810 was further refined by Pagé and Barnes (2009), has been applied to the average Seqi chromite
811 composition. This calculation suggests a parental melt compositions with approximately 13.0 wt.%
812 Al_2O_3 and 0.4 wt.% TiO_2 , which is similar to e.g. Troodos boninites (Cameron, 1985), as also
813 indicated by the U-shaped bulk-rock trace element patterns of the Seqi rocks (Fig. 7). However, the
814 chromite in MORB normalisation of Pagé and Barnes (2009) demonstrates that the Seqi chromites
815 are not of boninitic affinity (**Fig. D32** and **Fig. D33**), because of that the Seqi chromite is more
816 enriched in Al and Ti, although Mg and Cr are of the right order of magnitude.

817 Given that the Seqi dunites have undergone granulite-facies metamorphism and textural re-
818 equilibration it is impossible to estimate the initial amount of trapped interstitial liquid in these
819 cumulates. However, intercumulus liquid could potentially explain the U-shaped trace element
820 patterns (**Fig. 8**), where the most incompatible trace elements are elevated relative to an otherwise
821 positive slope of the HREE (Cawthorn et al., 1992). Nevertheless, given the highly magnesian
822 compositions of olivine and orthopyroxene at Seqi, it would appear unlikely that there was much
823 intercumulus liquid because this would have shifted the Mg# downwards, and required even more
824 magnesian compositions initially (Barnes, 1986).

825 The bulk-rock major element compositions of the Seqi rocks are adequately accounted for by the
826 measured compositions of olivine, orthopyroxene and spinel (**Fig. D34**). Only the metasomatic

827 amphibolite sample (186463) requires a component similar to the analysed amphibole, which likely
828 represents hydrated clinopyroxene as noted above. As a first order constraint on the trace element
829 composition of the melt from which the Seqi cumulates crystallized, the assumption that these rocks
830 represent adcumulates with no significant intercumulus was made and the procedure of Bédard
831 (1994) was tested via trace element inversion. An average composition of the homogeneous dunite
832 and the porphyritic dunites were used, because these are the most common rocks at Seqi and some
833 of the most depleted, which also suggests low levels of trapped interstitial melt. However, the
834 results of the modelling are not consistent with the observed trace element compositions of the Akia
835 terrane, because it would require an extremely trace element enriched parental magma (1000 times
836 chondritic LREE). Thus, either the partition coefficients of Bédard (1994) are not applicable to the
837 conditions under which the Seqi Ultramafic Complex formed (indeed the partition coefficient
838 values of Grégoire et al. (2000) are significantly different), or else significant amounts of trapped
839 interstitial melt were in fact present. Alternatively, the Seqi dunites have experienced a late
840 metasomatic overprint during the intrusion of the regional granitoid crust, which could potentially
841 explain their enrichment in the most incompatible trace elements.

842 Bulk-rock trace element reconstruction using the measured mineral compositions presented in
843 **Section 5.4** is also not capable of accounting for the most incompatible trace elements of Seqi
844 dunites using reasonable estimates of the amount of amphibole and/or trapped melt (**Fig. D35**). It
845 would appear that an external component with elevated Th, U, Ta, Nb, Ce, Hf and Zr is needed to
846 balance the trace element budget. However, granitoid crustal contaminant appears unlikely, because
847 it would be depleted in Ta and Nb. It seems more reasonable that the discrepancy between the
848 observed bulk-rock composition of the Seqi dunites and the integrated mineral compositions
849 measured by *in situ* LA-ICP-MS (see **Fig. D35**) could be accounted for by fractional liquids in the

850 interstices of the cumulate minerals. Late-stage melts would indeed become enriched in the most
851 incompatible trace elements, and remobilisation of this component would be capable of
852 overprinting the otherwise depleted cumulus phases (Cawthorn, 1992).

853 Orthopyroxene in these rocks may reflect the very high degrees of partial melting of the mantle
854 source region to the point of complete exhaustion, as also proposed for the regional SCLM
855 (Bernstein et al., 2007). Alternatively, orthopyroxene may reflect assimilation of a siliceous
856 component, because it is usually associated with chromitite, which may also have been induced to
857 crystallize by interaction of the primitive magma with crustal material (Irvine, 1977).

858 The frequent occurrence of orthopyroxene associated with the chromitite bands could either be a
859 secondary feature related to the oxidation of olivine to form magnetite and excess silica during
860 amphibolite-facies metamorphism (Irvine, 1967). The silica would then react with olivine to
861 produce orthopyroxene. Alternatively, the presence of orthopyroxene in association with chromitite
862 could reflect local crustal contamination, which could again add excess silica that would react with
863 olivine to form orthopyroxene. Any silica addition to the magma would also displace the liquid line
864 of descent into the stability field of chromite, which would then crystallize as monomineralic layers
865 (Irvine, 1977).

866 However, in the above scenario one would expect to see a compositional difference in between
867 orthopyroxene in the dunite and orthopyroxene in the chromitite. However, they are in fact the
868 same, both in terms of major and trace element abundances. Orthopyroxene therefore appears to be
869 the intercumulus phase formed by silica enrichment in the residual trapped liquids. This model
870 would explain the association of orthopyroxene with the chromitites, because spinel takes up no Si
871 and thus pushes the Si content of the intercumulus liquid up even faster than olivine crystallization
872 would. This could also explain why there is abundant orthopyroxene in the chromitites, when

873 compared to the dunites. Finally, Ni exchange equilibria between orthopyroxene and olivine are
874 identical for the dunites and chromitites (**Fig. 17**). Thus, orthopyroxene seems to be part of the
875 equilibrium assemblage of the Seqi Ultramafic Complex, if the Ni-thermometry indeed presents
876 only partially reset igneous temperatures, for orthopyroxene to have been an igneous phase (see
877 **Section 5.7**).

878 Mössbauer spectroscopic data on the Seqi chromitite yields $\text{Fe}^{3+}/\Sigma\text{Fe}$ of 0.157 to 0.209 (rejecting
879 one outlier). This narrow range in composition of chromitite is consistent with the observation that
880 there was no secular evolution in the oxidation state of Earth's mantle according to the recent study
881 by Rollinson et al. (2017). Of the chromitites that were measured by the Mössbauer technique one
882 sample (186469) has significantly higher $\text{Fe}^{3+}/\Sigma\text{Fe}$ (0.470). Given that most of the electron
883 microprobe data for spinel from the Seqi Ultramafic Complex plot below $\text{Fe}^{3+\#}$ of 20 (**Fig. 19**), the
884 more oxidised sample is likely to have been disturbed by either metamorphic fluids (Evans and
885 Frost, 1974), or by metasomatic fluids associated with the intrusion of the hosting granitoids. Lenaz
886 et al. (2014) reported oxidation of chromitites in the mantle section of Oman and ascribed this to an
887 association with ductile shear zones in harzburgite. They estimated the temperature of replacement
888 to be above that of ferritchromite stability but below 700 °C, which would also appear to be
889 reasonable conditions for the metasomatism of parts of the Seqi chromitites. However, it should be
890 stressed that the cores of chromite within the chromitites likely represent the most robust domains
891 of the Seqi Ultramafic Complex, because they would be strongly buffered. Chromite is thus the best
892 potential record of the primary igneous conditions in the Seqi rocks.

893 The *in situ* trace element data for amphibole in the Seqi rocks displaying negative anomalies for
894 Ta–Nb–Ti (**Fig. 13**), suggest that it represents igneous clinopyroxene that was later hydrated to
895 form amphibole during metamorphic hydration. These anomalies are typical for clinopyroxene, but

896 not for igneous amphibole due to significantly lower partition coefficients for these particular trace
897 elements in the latter (e.g., Tiepolo et al., 2007; Otamendi et al., 2016; Terentiev et al., 2016). This
898 interpretation is consistent with the pseudosection modelling (**Fig. 17**), although further studies of
899 the various settings of amphibole in the Seqi rocks are needed to better constrain the origin of this
900 particular mineral. Regardless of the origin, the negative Sr- and Eu-anomalies of the amphibole
901 points to equilibration with plagioclase, as is also suggested by the bulk-rock trace element data in
902 **Fig. 8**. This in turn points to a co-magmatic relationship with noritic cumulate rocks that are
903 commonly associated with peridotites in this region (Garde, 1997; Kristensen, 2006; Szilas et al.,
904 2015b).

905

906 **6.3. Petrogenetic model for the Seqi Ultramafic Complex**

907

908 Based on the presented data, the Seqi Ultramafic Complex represents a sequence of olivine-
909 dominated cumulates, rather than a mantle fragment. This is supported by the field observations of
910 repeated subparallel layers of chromitite, rhythmic layering and crossbedding of orthopyroxene
911 (Dahl, 2004), the presence of poikilitic orthopyroxene in peridotite, and the overall high modal
912 abundance of chromite (up to 12 vol.%) in the layered dunite, all of which indicates igneous crustal
913 processes that are not typical of mantle sections. As such, Seqi is similar to other mafic-ultramafic
914 intrusions derived from highly magnesian magmas (Barnes, 1989; Wooden et al., 1991; Maier et al.,
915 2000; Harris et al., 2005). The specific chromitite compositions are not compatible with a mantle
916 origin for the Seqi Ultramafic Complex as shown in **Fig. 12**.

917 Furthermore, **Fig. 19** demonstrates an affinity of the Seqi rocks with reduced layered intrusions
918 based on the overall chromite chemistry. However, we note that Révillon et al. (2000) proposed that

919 plutonic ultramafic rocks (dunites) associated with Phanerozoic komatiites on Gorgona Island,
920 represents the plumbing system of an oceanic plateau. A similar model may in fact also be viable
921 for the Seqi Ultramafic Complex, and this furthermore appears consistent with the observation that
922 supracrustal belts in SW Greenland commonly have cores of ultramafic cumulate rocks (e.g., Polat
923 et al., 2007; Szilas et al., 2014c, 2015a). This model needs further testing, because essentially all of
924 the Archaean supracrustal belts of SW Greenland have been proposed to have formed in a hydrous
925 subduction zone environment (e.g., Polat et al., 2011; Szilas et al., 2013b, 2014b; Furnes et al.,
926 2015). Yet it appears that the parental magma of the Seqi Ultramafic Complex was instead a dry
927 melt derived by large degrees of partial melting of the mantle, and so a direct link is not apparent
928 within the current paradigm for the Archaean of SW Greenland.

929 Given that the Seqi peridotites (*s.l.*) are not mantle rocks, but consistently have highly forsteritic
930 olivine compositions, it is likely that they represent the first formed cumulates, which were derived
931 by large degree melting of the mantle. The relatively high pressure of emplacement (~2GPa), yet
932 the complete lack of evidence for true mantle rocks, points to formation of the Seqi Ultramafic
933 Complex by crystal fractionation in the crust rather than in the mantle. An alternative model of
934 critical melting after the exhaustion of garnet in the mantle source (cf., Robin-Popieul et al., 2012)
935 may have relevance for the formation of the parental melt of the Seqi Ultramafic Complex. This
936 could potentially explain the dry and depleted nature of these cumulate rocks, although the viability
937 of this model also needs further detailed investigations to assess. Regardless of the exact parental
938 magma composition and the geotectonic setting, there appears to be robust field- and P - T evidence
939 for emplacement of the Seqi Ultramafic Complex within thick mafic-ultramafic crust that later
940 underwent partial melting to form the extensive regional TTG-suite crust that presently dominates
941 the craton.

942 Because the first formed olivine is essentially in equilibrium with its mantle source, one would
943 expect that the mantle residue from which the Seqi magma was extracted would be highly
944 refractory. This is consistent with the observation that much of the North Atlantic Craton is
945 underlain by unusually depleted sub-continental lithospheric mantle (SCLM) and indeed, it is worth
946 noting that similar olivine and spinel compositions are found in mantle xenoliths of the North
947 Atlantic Craton (cf., Bernstein et al., 1998, 2006, 2007, 2013; Wittig et al., 2008, 2010). This
948 remarkably depleted nature of the Archaean SCLM is to be expected given the greater potential
949 temperature of Earth's mantle during the Mesoarchaean Eon (e.g., Herzberg et al., 2010; Ganne
950 Feng, 2017).

951 A potential link between the Seqi peridotites and the regional SCLM has recently been proposed
952 based on the highly forsteritic and refractory nature of the Seqi dunites (Pearson et al., 2016; Szilas
953 et al., 2016b), which essentially overlaps in terms of bulk-rock major elements (**Fig D22**), and
954 because the incorporation of cumulate rocks may be able to explain some of the Fe-rich SCLM
955 xenoliths that are unlikely to represent mantle residues. The physical characteristics of the lower
956 crustal Seqi cumulate rocks would indeed be similar to those of the relatively buoyant residual
957 SCLM. Thus, Archaean dunite cumulates may contribute to the long-term development of SCLM
958 by density-driven sorting in the lithospheric mantle in a model similar to that proposed by Arndt et
959 al. (2002) or by Wang et al. (2016). However, in detail there are significant geochemical
960 discrepancies in terms of trace element compositions, as well as of PGE abundances ((**Fig. D23**,
961 **Fig. D24 and Fig. D25**) between Seqi-style cumulates and SCLM, which obviously needs to be
962 addressed by future studies.

963

964 7. Conclusions

965

966 The minimum age of the Seqi Ultramafic Complex is 2970 Ma, as defined by the hosting tonalitic
967 orthogneiss, as well as intrusive sheets of this age. The intrusion of this granitoid crust into the Seqi
968 Ultramafic Complex and has caused fragmentation of the ultramafic body. The peridotites (*s.l.*) of
969 the Seqi Ultramafic Complex consist mainly of dunite and do not represent mantle rocks, but were
970 rather a cumulate that was emplaced into thick mafic crust prior to the formation of the regional
971 TTG-suite crust. A cumulate origin is evident from field observations, the chromite compositions,
972 the highly forsteritic olivine, and the platinum-group element patterns, none of which are
973 comparable to fertile mantle lherzolite, depleted harzburgite or residual mantle dunite. Instead, the
974 Seqi peridotites represent olivine + spinel dominated cumulates, derived from a highly magnesian
975 magma with a relatively high Al/Ti and low Ca/Al ratios.

976 Mineral parageneses and exchange equilibria suggest emplacement as a relatively dry melt (\sim
977 $a_{\text{H}_2\text{O}} = 0.1$) at a pressure of less than 2.3 GPa followed by a metamorphic overprint in the mid- to
978 lower-crust at granulite facies conditions ($T = 700$ to 900°C , $P = 1.0$ to 2.4 GPa).

979 *In situ* LA-ICP-MS trace element data for amphibole in peridotite displays negative Ta–Nb–Ti
980 anomalies. We interpret this to imply metamorphic replacement of clinopyroxene, rather than
981 igneous amphibole, which is in agreement with the reduced and relatively dry conditions suggested
982 by chromite compositions and P – T estimates. However, it is noted that there are several different
983 types and settings of amphibole in the Seqi rocks, which needs further detailed investigations to
984 specifically assess their petrogenesis.

985 Oxides in the dunite are chromite with variable compositions ranging from Mg# of 15.4 to 62.9
986 and Cr# ranging from 26.4 to 97.4, whereas chromitite bands found within peridotite have tighter
987 spinel compositions with Mg# ranging from 33.7 to 50.5 and Cr# ranging from 55.7 to 70.1. Spinel

988 $\text{Fe}^{3+}\#$ is mostly below 20 for all lithological units in the Seqi Ultramafic Complex, which is
989 consistent with Mössbauer spectroscopic data of the chromitite yielding $\text{Fe}^{3+}/\Sigma\text{Fe}$ of mainly 0.157
990 to 0.209. The low $\text{Fe}^{3+}\#$ and moderate Mg# of the Seqi spinel, rule out an origin as an Alaskan-type
991 zoned complex, whereas the high Al/Ti, Ni/Cu and low Gd_N/Yb_N and Pd/Ru are not consistent with
992 a komatiitic affinity either. Thus, bulk-rock major, trace and platinum-group element data does not
993 support a komatiitic affinity of the Seqi rocks, despite their highly forsteritic olivine compositions
994 and an alternative geodynamic setting could be an oceanic plateau.

995 The Seqi crustal cumulate rocks have negative bulk-rock Eu–Sr-anomalies, which indicates a co-
996 magmatic relationship with noritic cumulate rocks, which are found associated with similar mafic-
997 ultramafic complexes in the Fiskefjord region (Garde, 1997; Kristensen, 2006; Szilas et al. 2015b).

998 Elevated bulk-rock Th and U in combination with low Nb/La either indicates: (1) crustal
999 contamination of the mantle source region of the primary magma of the Seqi Ultramafic Complex
1000 (boninite-style magmatism), or (2) continental crustal assimilation during the intrusion of the Seqi
1001 complex into basement that existed prior to the current regional orthogneiss terrane, or (3)
1002 alternatively metasomatic overprinting during the late intrusion of the hosting TTG-suite granitoids.
1003 These different models are not distinguishable with the currently available geochemical data and
1004 thus future isotope studies are needed on these rocks.

1005 Collectively, the highly forsteritic olivine and elevated bulk-rock IPGE abundances point to very
1006 hot conditions during the melt extraction from the mantle. The chromite compositions of the Seqi
1007 Ultramafic Complex are comparable to those of reduced layered intrusions (or magma conduits).
1008 This further suggests that the Seqi cumulates rocks were derived from a primary magma that
1009 formed by very large degrees (>40%) of partial melting of the mantle source. We note that such
1010 mantle residues could potentially represent the current SCLM of this region, which warrants further

1011 investigation to test this possibility, as it could have global implications for the understanding of
1012 craton formation.

1013

1014 **Acknowledgements**

1015

1016 K. Szilas would like to thank Graham Pearson and Tomoaki Morishita for fruitful discussion during
1017 fieldwork in Greenland, which helped develop a better understanding of the peridotites of the
1018 Fiskefjord region. Jarl Boyd is acknowledged for assistance during the rock sampling at the Seqi
1019 Ultramafic Complex. Comments on an early version of the manuscript by Nick Arndt, Ole Dahl,
1020 Dmitri Ionov, Troels Nielsen and Marc Norman are appreciated. Editorial handling of the
1021 manuscript by Sohini Ganguly is acknowledged. The authors greatly appreciate thorough reviews
1022 by Tomoaki Morishita and Riccardo Tribuzio, which significantly improved the resulting paper.
1023 Financial support to K. Szilas from Knud Højgaards Fond for the fieldwork at the Seqi Ultramafic
1024 Complex, and research grant VKR023371 from VILLUM FOUNDATION and research grant CF16-
1025 0059 from CARLSBERG FOUNDATION made this study possible.

1026

1027 **References**

1028

1029 Arai, T., Omori, S., Komiya, T., Maruyama, S., 2015. Intermediate P/T-type regional
1030 metamorphism of the Isua Supracrustal Belt, southern west Greenland: The oldest Pacific-type
1031 orogenic belt? *Tectonophysics* 662, 22–39.

1032

1033 Arndt, N.T., Lewin, É., Albarède, F., 2002. Strange partners: formation and survival of continental

- 1034 crust and lithospheric mantle. Geological Society, London, Special Publications 199, 91–103.
- 1035
- 1036 Arndt, N., Leshar, C.M. , Barnes, S J., 2008. Komatiite. Cambridge University Press, New York.
- 1037 ISBN: 978-0521874-748, 488 pp.
- 1038
- 1039 Asmund, G., Boertmann, D. , Johansen, P., 2009. Baseline and monitoring studies at the Seqi mine
- 1040 2004 to 2007. National Environmental Research Institute, NERI Technical Report No. 715, Aarhus
- 1041 University, Denmark, 90 pp.
- 1042
- 1043 Ballhaus, C., Berry, R.F., Green, D.H., 1991. High pressure experimental calibration of the olivine–
- 1044 orthopyroxene–spinel oxygen geobarometer: implications for the oxidation state of the mantle.
- 1045 Contributions to Mineralogy and Petrology 107, 27–40
- 1046
- 1047 Ballhaus, C., 1998. Origin of podiform chromite deposits by magma mingling. Earth and Planetary
- 1048 Science Letters 156, 185–193.
- 1049
- 1050 Barnes, S.J., 1986. The effect of trapped liquid crystallization on cumulus mineral compositions in
- 1051 layered intrusions. Contributions to Mineralogy and Petrology 93, 524–531.
- 1052
- 1053 Barnes, S. J. , Fiorentini, M. L., 2008. Iridium, ruthenium and rhodium in komatiites: evidence for
- 1054 iridium alloy saturation. Chemical Geology 257, 44–58.
- 1055
- 1056 Barnes, S.J., 1989. Are Bushveld U-type parent magmas boninites or contaminated komatiites?

- 1057 Contributions to Mineralogy and Petrology 101, 447–457.
- 1058
- 1059 Barnes, S.J., Roeder, P.L., 2001. The range of spinel compositions in terrestrial mafic and
1060 ultramafic rocks. *Journal of Petrology* 42, 2279–2302.
- 1061
- 1062 Becker, H., Horan, M.F., Walker, R.J., Gao, S., Lorand, J.P., Rudnick, R.L., 2006. Highly
1063 siderophile element composition of the Earth's primitive upper mantle: constraints from new data
1064 on peridotite massifs and xenoliths. *Geochimica et Cosmochimica Acta* 70, 4528–4550.
- 1065
- 1066 Bédard, J.H., 1994. A procedure for calculating the equilibrium distribution of trace elements
1067 among the minerals of cumulate rocks, and the concentration of trace elements in the coexisting
1068 liquids. *Chemical Geology* 118, 143–153.
- 1069
- 1070 Begg, G.C., Hronsky, J.A., Arndt, N.T., Griffin, W.L., O'Reilly, S.Y., Hayward, N., 2010.
1071 Lithospheric, cratonic, and geodynamic setting of Ni-Cu-PGE sulfide deposits. *Economic Geology*
1072 105, 1057–1070.
- 1073
- 1074 Bennett, V.C., Nutman, A.P., Esat, T.M., 2002. Constraints on mantle evolution from $^{187}\text{Os}/^{188}\text{Os}$
1075 isotopic compositions from Archaean ultramafic rocks from southern west Greenland (3.8 Ga) and
1076 western Australia (3.46 Ga). *Geochimica et Cosmochimica Acta* 66, 2615–2630.
- 1077
- 1078 Bernstein, S., Kelemen, P.B., Brooks, C.K., 1998. Depleted spinel harzburgite xenoliths in Tertiary
1079 dykes from East Greenland: restites from high degree melting. *Earth and Planetary Science Letters*

1080 154, 221–235.

1081

1082 Bernstein, S., Hanghøj, K., Kelemen, P.B. , Brooks, C.K., 2006. Ultra-depleted, shallow cratonic
1083 mantle beneath West Greenland: dunitic xenoliths from Ubekendt Ejland. Contributions to
1084 Mineralogy and Petrology 152, 335–347.

1085

1086 Bernstein, S., Kelemen, P. B. , Hanghøj, K., 2007. Consistent olivine Mg# in cratonic mantle
1087 reflects Archean mantle melting to the exhaustion of orthopyroxene. Geology 35, 459–462.

1088

1089 Bernstein, S., Szilas, K., Kelemen, P.B., 2013. Highly depleted cratonic mantle in West Greenland
1090 extending into diamond stability field in the Proterozoic. Lithos 168, 160–172.

1091

1092 Bodinier, J.L., Godard, M., 2003. Orogenic, ophiolitic, and abyssal peridotites. Treatise on
1093 Geochemistry 2, 568 pp.

1094

1095 Bridgwater, D., McGregor, V. R., Myers, J.S., 1974. A horizontal tectonic regime in the Archaean
1096 of Greenland and its implications for early crustal thickening. Precambrian Research 1, 179–197.

1097

1098 Brey, G.P., Köhler, T., 1990. Geothermobarometry in four-phase Lherzolites II. New
1099 thermobarometers and practical assessment of existing thermobarometers. Journal of Petrology 31,
1100 1353–1378.

1101

1102 Burns, L.E., 1985. The Border Ranges ultramafic and mafic complex, south-central Alaska:

- 1103 cumulate fractionates of island-arc volcanics. *Canadian Journal of Earth Sciences* 22, 1020–1038.
1104
- 1105 Cameron, E.N., 1978. The lower zone of the eastern Bushveld Complex in the Olifants River
1106 trough. *Journal of Petrology* 19, 437–462.
1107
- 1108 Cameron, W.E., 1985. Petrology and origin of primitive lavas from the Troodos ophiolite, Cyprus.
1109 *Contributions to Mineralogy and Petrology* 89, 239–255.
1110
- 1111 Cawthorn, R.G., Sander, B.K. , Jones, I.M., 1992. Evidence for the trapped liquid shift effect in the
1112 Mount Ayliff Intrusion, South Africa. *Contributions to Mineralogy and Petrology* 111, 194–202.
1113
- 1114 Cawthorn, R.G. (Ed.), 1996. *Layered intrusions*. Elsevier, New York, 531 pp.
1115
- 1116 Christiansen, O., 1997. The Seqinnersuaq olivine deposit southern West Greenland – A review of
1117 geological and technical information. NunaOil A/S company report. GEUS report file 21628, 137
1118 pp.
1119
- 1120 Christiansen, O., 1998. The Seqinnersuaq olivine deposit southern West Greenland – preliminary
1121 magnetic separation tests. NunaOil A/S company report. GEUS report file 21625, 8 pp.
1122
- 1123 Colás, V., Gonzalez-Jimenez, J.M., Griffin, W.L., Fanlo, I., Gervilla, F., O'Reilly, S.Y., Pearson,
1124 N.J., Kerestedjian, T. , Proenza J.A., 2014. Fingerprints of metamorphism in chromite: New
1125 insights from minor and trace elements. *Chemical Geology* 389, 137–152.

1126

1127 Connolly, J.A.D., 2005. Computation of phase equilibria by linear programming: A tool for
1128 geodynamic modeling and its application to subduction zone decarbonation. *Earth and Planetary
1129 Science Letters* 236, 524–541.

1130

1131 Dahl, O., 2004. Seqi olivine deposit report 2003. Crew Gold Corporation report for Bureau of
1132 Minerals and Petroleum (BMP), 94 pp.

1133

1134 de Hoog, J.C.M., Gall L. , Cornell D.H., 2010. Trace-element geochemistry of mantle olivine and
1135 application to mantle petrogenesis and geothermobarometry. *Chemical Geology* 270, 196–215.

1136

1137 Diener, J., Powell, R., 2012. Revised activity–composition models for clinopyroxene and
1138 amphibole. *Journal of Metamorphic Geology* 30, 131–142

1139

1140 Downes, H., 2001. Formation and modification of the shallow sub-continental lithospheric mantle:
1141 a review of geochemical evidence from ultramafic xenolith suites and tectonically emplaced
1142 ultramafic massifs of western and central Europe. *Journal of Petrology* 42, 233–250.

1143

1144 Dyck, B., Reno, B.L. , Kokfelt, T.F., 2015. The Majorqaq Belt: A record of Neoproterozoic
1145 orogenesis during final assembly of the North Atlantic Craton, southern West Greenland. *Lithos*
1146 220, 253–271.

1147

1148 Dziggel, A., Diener, J.F. A., Kolb, J. , Kokfelt, T.F., 2014. Metamorphic record of accretionary

1149 processes during the Neoproterozoic: The Nuuk region, southern West Greenland. *Precambrian*
1150 *Research* 242, 22–38.

1151

1152 Eales, H.V. , Cawthorn, R.G., 1996. The bushveld complex. *Developments in Petrology* 15, 181–
1153 229.

1154

1155 Evans, B.W. , Frost, B.R., 1974. Chrome-spinel in progressive metamorphism - a preliminary
1156 analysis. *Geochimica et Cosmochimica Acta* 39, 959–972.

1157

1158 Fiorentini, M.L., Barnes, S.J., Maier, W.D., Burnham, O.M., Heggie, G., 2011. Global variability in
1159 the platinum-group element contents of komatiites. *Journal of Petrology* 52, 83–112.

1160

1161 Fisher-Gödde, M., Becker, H., Wombacher, F., 2010. Rhodium, gold and other highly siderophile
1162 element abundances in chondritic meteorites. *Geochimica et Cosmochimica Acta* 74, 356–379.

1163

1164 Frei, D. , Gerdes, A., 2009. Precise and accurate in situ U–Pb dating of zircon with high sample
1165 throughput by automated LA-SF-ICP-MS. *Chemical Geology* 261, 261–270.

1166

1167 Friend, C.R.L., Bennett, V.C. , Nutman, A.P., 2002. Abyssal peridotites >3,800 Ma from southern
1168 west Greenland: field relationships, petrography, geochronology, whole-rock and mineral chemistry
1169 of dunite and harzburgite inclusions in the Itsaq Gneiss Complex. *Contributions to Mineralogy and*
1170 *Petrology* 143, 71–92.

1171

1172 Friend, C.R. , Nutman, A.P., 2005. New pieces to the Archaean terrane jigsaw puzzle in the Nuuk
1173 region, southern West Greenland: steps in transforming a simple insight into a complex regional
1174 tectonothermal model. *Journal of the Geological Society* 162, 147–162.

1175

1176 Friend, C.R. , Nutman, A.P., 2010. Eoarchean ophiolites? New evidence for the debate on the Isua
1177 supracrustal belt, southern West Greenland. *American Journal of Science* 310, 826–861.

1178

1179 Furnes, H., Dilek, Y., De Wit, M., 2015. Precambrian greenstone sequences represent different
1180 ophiolite types. *Gondwana Research* 27, 649–685.

1181

1182 Ganne, J. , Feng, X. 2017. Primary magmas and mantle temperatures through time. *Geochemistry,*
1183 *Geophysics, Geosystems* 18, 2016GC006787.

1184

1185 Gannoun, A., Burton, K.W., Day, J.M., Harvey, J., Schiano, P. , Parkinson, I., 2016. Highly
1186 siderophile element and Os isotope systematics of volcanic rocks at divergent and convergent plate
1187 boundaries and in intraplate settings. *Reviews in Mineralogy and Geochemistry* 81, 651–724.

1188

1189 Garde, A.A., 1997. Accretion and evolution of an Archaean high-grade grey gneiss–amphibolite
1190 complex: the Fiskefjord area, southern West Greenland. *Geology of Greenland Survey Bulletin* 177,
1191 115 pp.

1192

1193 Garde, A.A., 2007. A mid-Archaean island arc complex in the eastern Akia terrane, Godthåbsfjord,
1194 southern West Greenland. *Journal of the Geological Society* 164, 565–579.

1195

1196 Garde, A.A., Whitehouse, M., Christensen, R., 2012. Mesoarchean epithermal gold mineralization
1197 preserved at upper amphibolite-facies grade, Qussuk, southern West Greenland. *Economic Geology*
1198 107, 881–908.

1199

1200 Garde, A.A., Dyck, B., Esbensen, K.H., Johansson, L. , Möller, C., 2015. The Finnefjeld domain,
1201 Maniitsoq structure, West Greenland: Differential rheological features and mechanical
1202 homogenisation in response to impacting? *Precambrian Research* 255, 791–808.

1203

1204 Gerdes, A. , Zeh, A., 2006. Combined U-Pb and Hf isotope LA-(MC)-ICP-MS analyses of detrital
1205 zircons: Comparison with SHRIMP and new constraints for the provenance and age of an
1206 Armorican metasediment in Central Germany. *Earth and Planetary Science Letters* 249. 47–61.

1207

1208 Grégoire, M., Moine, B.N., O'Reilly, S.Y. , Giret A., 2000. Trace Element Residence and
1209 Partitioning in Mantle Xenoliths Metasomatized by Highly Alkaline, Silicate- and Carbonate-rich
1210 Melts (Kerguelen Islands, Indian Ocean). *Journal of Petrology* 41, 477–509.

1211

1212 Groves, D.I. , Bierlein, F.P., 2007. Geodynamic settings of mineral deposit systems. *Journal of the*
1213 *Geological Society* 164, 19–30.

1214

1215 Hanghøj, K., Kelemen, P.B., Hassler, D. , Godard, M., 2010. Composition and genesis of depleted
1216 mantle peridotites from the Wadi Tayin Massif, Oman Ophiolite; major and trace element
1217 geochemistry, and Os isotope and PGE systematics. *Journal of Petrology* 51, 201–227.

1218

1219 Hanmer, S. , Greene, D.C., 2002. A modern structural regime in the Paleoproterozoic (~ 3.64 Ga); Isua
1220 Greenstone Belt, southern West Greenland. *Tectonophysics* 346, 201–222.

1221

1222 Harris, C., Pronost, J.J., Ashwal, L.D. , Cawthorn, R.G., 2005. Oxygen and hydrogen isotope
1223 stratigraphy of the Rustenburg Layered Suite, Bushveld Complex: constraints on crustal
1224 contamination. *Journal of Petrology* 46, 579–601.

1225

1226 Hattori, K., Hart, S.R., 1997. PGE and Os isotopic signatures for ultramafic rocks from the base of
1227 the Talkeetna island arc, Alaska. *EOS* 78, 339.

1228

1229 Hattori, K. , Shirahase, T., 1997. Platinum group elements and osmium isotope signatures of the
1230 Kohistan island arc sequence, Himalaya-Karakoram area. *EOS* 78, 829.

1231

1232 Hattori, K.H. , Guillot, S., 2007. Geochemical character of serpentinites associated with high-to
1233 ultrahigh-pressure metamorphic rocks in the Alps, Cuba, and the Himalayas: Recycling of elements
1234 in subduction zones. *Geochemistry, Geophysics, Geosystems*, 8, 2007GC001594.

1235

1236 Hawthorne, F.C., Oberti, R., Harlow, G.E., Maresch, W.V., Martin, R.F., Schumacher, J.C., Welch,
1237 M.D., 2012. Nomenclature of the amphibole supergroup. *American Mineralogist* 97, 2031–2048.

1238

1239 Herzberg, C., Condie, K. , Korenaga, J., 2010. Thermal history of the Earth and its petrological
1240 expression. *Earth and Planetary Science Letters* 292, 79–88.

1241

1242 Holland T.J.B. , Powell, R., 2011. An improved and extended internally consistent thermodynamic
1243 dataset for phases of petrological interest, involving a new equation of state for solids. *Journal of*
1244 *Metamorphic Geology* 29, 333–383.

1245

1246 Huber, H., Koeberl, C., McDonald, I. , Reimold, W.U., 2001. Geochemistry and petrology of
1247 Witwatersrand and Dwyka diamictites from South Africa: search for an extraterrestrial component.
1248 *Geochimica et Cosmochimica Acta* 65, 2007–2016.

1249

1250 Irvine, T.N., 1967. Chromian spinel as a petrogenetic indicator. Part 2. Petrologic applications.
1251 *Canadian Journal of Earth Sciences*, Vol. 4, 71–103.

1252

1253 Irvine, T.N., 1974. Petrology of the Duke Island ultramafic complex southeastern Alaska.
1254 *Geological Society of America Memoirs* 138, 1–244.

1255

1256 Irvine, T.N., 1977. Origin of chromitite layers in the Muskox intrusion and other stratiform
1257 intrusions: a new interpretation. *Geology* 5, 273–277.

1258

1259 Jackson, S., Pearson, N.J., Griffin, W.L. , Belousova, E.A., 2004. The application of laser ablation -
1260 inductively coupled plasma - mass spectrometry to in situ U–Pb zircon geochronology. *Chemical*
1261 *Geology* 211, 47–69.

1262

1263 Janošek, V., Farrow, C.M. , Erban, V., 2006. Interpretation of whole-rock geochemical data in

- 1264 igneous geochemistry: introducing Geochemical Data Tool (GCDkit). *Journal of Petrology* 47,
1265 1255–1259.
- 1266
- 1267 Jenner, F.E., Bennett, V.C., Nutman, A.P., Friend, C.R.L., Norman, M.D. , Yaxley, G., 2009.
1268 Evidence for subduction at 3.8 Ga: Geochemistry of arc-like metabasalts from the southern edge of
1269 the Isua Supracrustal Belt. *Chemical Geology* 261, 83–98.
- 1270
- 1271 Jenner, F., Bennett, V., Yaxley, G., Friend, C. , Nebel, O., 2014. Eoarchean within-plate basalts
1272 from southwest Greenland. *Geology* 42, 331–331.
- 1273
- 1274 Jennings, E.S. , Holland, T.J.B., 2015. A Simple Thermodynamic Model for Melting of Peridotite
1275 in the System NCFMASOCr. *Journal of Petrology* 56, 869–892.
- 1276
- 1277 Kelemen, P.B., Dick, H.J.B., Quick, J.E., 1992. Formation of harzburgite by pervasive melt/rock
1278 reaction in the upper mantle. *Nature* 358, 635–641.
- 1279
- 1280 Keulen, N., Schumacher, J.C., Næraa, T., Kokfelt, T.F., Scherstén, A., Szilas, K., van Hinsberg,
1281 V.J., Schlatter, D.M., Windley, B.F., 2014. Meso- and Neoproterozoic geological history of the
1282 Bjørnesund and Ravens Storø Supracrustal Belts, southern West Greenland: Settings for gold
1283 enrichment and corundum formation. *Precambrian Research* 254, 36–58.
- 1284
- 1285 Kisters, A.F.M., van Hinsberg, V.J., Szilas, K., 2012. Geology of an Archaean accretionary
1286 complex – The structural record of burial and return flow in the Tartoq Group of South West

- 1287 Greenland. *Precambrian Research* 220, 107–122.
- 1288
- 1289 Kolb, J., Kokfelt, T.F., Dziggel, A., 2012. Geodynamic setting and deformation history of an
1290 Archaean terrane at mid-crustal level: The Tasiusarsuaq terrane of southern West Greenland.
1291 *Precambrian Research* 212, 34–56.
- 1292
- 1293 Kristensen, T., 2006. En geologisk og geokemisk tolkning af mafiske og ultramafiske bjergarter og
1294 deres økonomiske mineralpotentiale, Fiskefjordsregionen, sydlige Vestgrønland. Unpublished
1295 M.Sc. thesis, Aarhus University, 135 pp.
- 1296
- 1297 Kusky, T.M., Li, J.H., Tucker, R.D., 2001. The Archean Dongwanzi ophiolite complex, North China
1298 Craton: 2.505-billion-year-old oceanic crust and mantle. *Science* 292, 1142–1145.
- 1299
- 1300 Le Maitre, R.W., Streckeisen, A., Zanettin, B., Le Bas, M.J., Bonin, B., Bateman, P. (Eds.), 2005.
1301 *Igneous rocks: a classification and glossary of terms: recommendations of the International Union
1302 of Geological Sciences Subcommittee on the Systematics of Igneous Rocks*. Cambridge
1303 University Press, 254 pp.
- 1304
- 1305 Lenaz, D., Adetunji, J., Rollinson, H., 2014. Determination of $Fe^{3+}/\Sigma Fe$ ratios in chrome spinels
1306 using a combined Mössbauer and single-crystal X-ray approach: application to chromitites from the
1307 mantle section of the Oman ophiolite. *Contributions to Mineralogy and Petrology* 167, 1–17.
- 1308
- 1309 Liermann, H.P., Ganguly, J., 2003. Fe-Mg fractionation between orthopyroxene and spinel:

- 1310 Experimental calibration in the system FeO–MgO–Al₂O₃–Cr₂O₃–SiO₂, and applications.
1311 Contributions to Mineralogy and Petrology 145, 217–227.
1312
- 1313 Lindsley, D.H., 1983. Pyroxene thermometry. American Mineralogist 68, 477–493.
1314
- 1315 Lindsley, D.H., Andersen, D.J., 1983. A two-pyroxene thermometer. Journal of Geophysical
1316 Research: Solid Earth 88(S02).
1317
- 1318 Ludwig, K.R., 2012. Using Isoplot/Ex, version 3.76, A Geochronological Toolkit for Microsoft
1319 Excel. Berkeley Geochronology Center Special Publication 6.
1320
- 1321 Luguet, A., Shirey, S.B., Lorand, J.P., Horan, M.F., Carlson, R.W., 2007. Residual platinum-group
1322 minerals from highly depleted harzburgites of the Lherz massif (France) and their role in HSE
1323 fractionation of the mantle. Geochimica et Cosmochimica Acta 71, 3082–3097.
1324
- 1325 McBirney, A.R., 1996. The Skaergaard intrusion. Developments in Petrology 15, 147–180.
1326
- 1327 McDonald, I., Viljoen, K.S., 2013. Platinum-group element geochemistry of mantle eclogites: a
1328 reconnaissance study of xenoliths from the Orapa kimberlite, Botswana. Applied Earth Science:
1329 Transactions of the Institutions of Mining and Metallurgy, Section B.
1330
- 1331 Mai, H.N., 1998. Seqinnersuaq olivine deposit – Pre-feasibility study, technical description and
1332 cost estimation. NunaOil A/S company report. GEUS report file 21627, 27 pp.

1333

1334 Maier, W.D., Arndt, N.T., Curl, E.A., 2000. Progressive crustal contamination of the Bushveld
1335 Complex: evidence from Nd isotopic analyses of the cumulate rocks. *Contributions to Mineralogy
1336 and Petrology* 140, 316–327.

1337

1338 Maier, W.D., 2005. Platinum-group element (PGE) deposits and occurrences: mineralization styles,
1339 genetic concepts, and exploration criteria. *Journal of African Earth Sciences* 41, 165–191.

1340

1341 Maier W.D., Peltonen P., McDonald I., Barnes S.J., Barnes S.J., Hatton C., Viljoen F., 2012. The
1342 concentration of platinum-group elements and gold in southern African and Karelian kimberlite-
1343 hosted mantle xenoliths: Implications for the noble metal content of the Earth's mantle. *Chemical
1344 Geology* 302–303, 119–135.

1345

1346 Mathison, C.I., Ahmat, A.L., 1996. The Windimurra Complex, Western Australia. *Developments in
1347 Petrology* 15, 485–510.

1348

1349 Maurel, C., Maurel, P., 1982. Experimental study of the solubility of chromium in basic silicate
1350 melts and its distribution between liquid and coexistent minerals – conditions of existence of
1351 chromian spinel. *Bulletin de Mineralogie* 105, 640–647.

1352

1353 McBirney, A.R., Noyes, R.M., 1979. Crystallization and layering of the Skaergaard intrusion.
1354 *Journal of Petrology* 20, 487–554.

1355

- 1356 McCallum, I.S., 1996. The stillwater complex. *Developments in Petrology* 15, 441–483.
1357
- 1358 McCallum, I.S., Raedeke, L.D., Mathez, E.A., 1980. Investigations of the Stillwater Complex: Part
1359 I. Stratigraphy and structure of the Banded zone. *American Journal of Science* 280, 59–87.
1360
- 1361 Myers, J.S., 1976. Channel deposits of peridotite, gabbro and chromitite from turbidity currents in
1362 the stratiform Fiskenæsset anorthosite complex, southwest Greenland. *Lithos* 9, 281–291.
1363
- 1364 Naldrett, A.J., 1999. World-class Ni-Cu-PGE deposits: key factors in their genesis. *Mineralium*
1365 *Deposita* 34, 227–240.
1366
- 1367 Nielsen, T.F., Andersen, J.Ø., Holness, M.B., Keiding, J.K., Rudashevsky, N.S., Rudashevsky,
1368 V.N., Veksler, I.V., 2015. The Skaergaard PGE and gold deposit: the result of in situ fractionation,
1369 sulphide saturation, and magma chamber-scale precious metal redistribution by immiscible Fe-rich
1370 melt. *Journal of Petrology* 56, 1643–1676.
1371
- 1372 Niu, Y., 2004. Bulk-rock major and trace element compositions of abyssal peridotites: implications
1373 for mantle melting, melt extraction and post-melting processes beneath mid-ocean ridges. *Journal of*
1374 *Petrology* 45, 2423–2458.
1375
- 1376 Nutman, A.P., McGregor, V.R., Friend, C.R.L., Bennett, V.C., Kinny, P.D., 1996. The Itsaq Gneiss
1377 Complex of southern West Greenland; the world's most extensive record of early crustal evolution
1378 (3900–3600Ma). *Precambrian Research* 78, 1–39.

1379

1380 Nutman, A.P., Friend, C.R., 2007. Adjacent terranes with ca. 2715 and 2650Ma high-pressure
1381 metamorphic assemblages in the Nuuk region of the North Atlantic Craton, southern West
1382 Greenland: Complexities of Neoproterozoic collisional orogeny. *Precambrian Research* 155, 159–203.

1383

1384 Otamendi, J.E., Tiepolo, M., Walker, B.A., Cristofolini, E.A., Tibaldi, A.M., 2016. Trace elements
1385 in minerals from mafic and ultramafic cumulates of the central Sierra de Valle Fértil, Famatinian
1386 arc, Argentina. *Lithos* 240, 355–370.

1387

1388 Pagé, P., Barnes, S.J., 2009. Using trace elements in chromites to constrain the origin of podiform
1389 chromitites in the Thetford Mines ophiolite, Québec, Canada. *Economic Geology* 104, 997–1018.

1390

1391 Pagé, P., Barnes, S.J., 2016. The influence of chromite on osmium, iridium, ruthenium and rhodium
1392 distribution during early magmatic processes. *Chemical Geology* 420, 51–68.

1393

1394 Pal, T., Moon, H., Mitra, S., 1994. Distribution of iron cations in natural chromites at different
1395 stages of oxidation – A ^{57}Fe Mössbauer investigation. *J. Geol. Soc. India* 44, 234–243.

1396

1397 Palme, H., O'Neill, H.C., 2003. Compositional estimates of mantle composition. In: Carlson, R.W.
1398 (Ed.), *The Mantle and Core*, Vol. 2. In: Holland, H.D., Turekian, K.K., (Eds.), *Treatise on*
1399 *Geochemistry*. Elsevier-Pergamon, Oxford, UK, 1–38.

1400

1401 Paton, C., Hellstrom, J., Paul, B., Woodhead, J., Hergt, J., 2011. Iolite: Freeware for the

1402 visualisation and processing of mass spectrometric data. *Journal of Analytical Atomic Spectrometry*
1403 26, 2508–2518.

1404

1405 Pearson, D.G., Irvine, G.J., Ionov, D.A., Boyd, F.R., Dreibus, G.E., 2004. Re–Os isotope
1406 systematics and platinum group element fractionation during mantle melt extraction: a study of
1407 massif and xenolith peridotite suites. *Chemical Geology* 208, 29–59.

1408

1409 Pearson, D.G., Wang, H., van Hunen, J., Szilas, K., 2016. Making the complex mantle keels
1410 beneath cratons. *Goldschmidt Conference, Yokohama.*

1411 <https://goldschmidt.info/2016///uploads/abstracts/finalPDFs/2457.pdf>

1412

1413 Petrus, J.A., Kamber, B.S., 2012. *VizualAge: A Novel Approach to Laser Ablation ICP-MS U-Pb*
1414 *Geochronology Data Reduction*. *Geostandards and Geoanalytical Research* 36, 247–270.

1415

1416 Polat, A., Hofmann, A.W., Rosing, M.T., 2002. Boninite-like volcanic rocks in the 3.7–3.8 Ga Isua
1417 greenstone belt, West Greenland: geochemical evidence for intra-oceanic subduction zone
1418 processes in the early Earth. *Chemical Geology* 184, 231–254.

1419

1420 Polat, A., Appel, P.W., Frei, R., Pan, Y., Dilek, Y., Ordóñez-Calderón, J.C., Raith, J.G., 2007. Field
1421 and geochemical characteristics of the Mesoarchean (~ 3075Ma) Ivisartoq greenstone belt,
1422 southern West Greenland: Evidence for seafloor hydrothermal alteration in supra-subduction
1423 oceanic crust. *Gondwana Research* 11, 69–91.

1424

1425 Polat, A., Appel, P. W., Fryer, B.J., 2011. An overview of the geochemistry of Eoarchean to
1426 Mesoarchean ultramafic to mafic volcanic rocks, SW Greenland: implications for mantle depletion
1427 and petrogenetic processes at subduction zones in the early Earth. *Gondwana Research* 20, 255–
1428 283.

1429

1430 Polat, A., Wang, L., Appel, P. W., 2015. A review of structural patterns and melting processes in
1431 the Archean craton of West Greenland: Evidence for crustal growth at convergent plate margins as
1432 opposed to non-uniformitarian models. *Tectonophysics* 662, 67–94.

1433

1434 Povdin, P., 1988. Ni–Mg partitioning between synthetic olivines and orthopyroxene: applications to
1435 geothermometry. *American Mineralogist* 73, 274–280.

1436

1437 Prescher, C., McCammon, C., Dubrovinsky, L., 2012. MossA: a program for analyzing energy-
1438 domain Mössbauer spectra from conventional and synchrotron sources. *Journal of Applied*
1439 *Crystallography* 45, 329–331.

1440

1441 Quintiliani, M., 2005. Fe-57 Mossbauer spectroscopy analysis of spinels: Fe³⁺/Fe-tot quantification
1442 accuracy and consequences on f(O₂) estimate. *Periodico di Mineralogia* 74, 139–146.

1443

1444 Rais, A., Yousif, A.A., Al-shihi, M.H., Al-rawas, A.D., Gismelseed, A.M., El-zain, M.E., 2003.
1445 Cation distribution and magnetic properties of natural chromites. *Physica Status Solidi (b)* 239,
1446 439–446.

1447

- 1448 Révillon, S., Arndt, N.T., Chauvel, C., Hallot, E., 2000. Geochemical study of ultramafic volcanic
1449 and plutonic rocks from Gorgona Island, Colombia: the plumbing system of an oceanic plateau.
1450 *Journal of Petrology* 41, 1127–1153.
- 1451
- 1452 Robin-Popieul, C.C., Arndt, N.T., Chauvel, C., Byerly, G.R., Sobolev, A.V., Wilson, A., 2012. A
1453 new model for Barberton komatiites: deep critical melting with high melt retention. *Journal of*
1454 *Petrology* 53, 2191–2229.
- 1455
- 1456 Roeder, P.L., Emslie, R., 1970. Olivine-liquid equilibrium. *Contributions to Mineralogy and*
1457 *Petrology* 29, 275–289.
- 1458
- 1459 Rollinson, H., Appel, P.W.U., Frei, R., 2002. A metamorphosed, Early Archaean chromitites from
1460 West Greenland: implications for the genesis of Archaean anorthositic chromitites. *Journal of*
1461 *Petrology* 43, 2143–2170.
- 1462
- 1463 Rollinson, H., 2005. Chromite in the mantle section of the Oman ophiolite: a new genetic model.
1464 *Island Arc* 14, 542–550.
- 1465
- 1466 Rollinson, H., 2007. Recognising early Archaean mantle: a reappraisal. *Contributions to*
1467 *Mineralogy and Petrology* 154, 241–252.
- 1468
- 1469 Rollinson H.R., Adetunji, J., Yousif, A.A., Gismelseed, A.M., 2012. New Mössbauer measurements
1470 of $\text{Fe}^{3+}/\Sigma\text{Fe}$ in chromites from the mantle section of the Oman ophiolite: evidence for the oxidation

- 1471 of the sub-oceanic mantle. *Mineralogical Magazine* 76, 596–597.
- 1472
- 1473 Rollinson, H.R., Adetunji, J., Lenaz, D., Szilas, K., 2017. Archaean chromitites show constant
1474 $\text{Fe}^{3+}/\Sigma\text{Fe}$ in Earth's asthenospheric mantle since 3.8 Ga. *Lithos* 282, 316–325..
- 1475
- 1476 Rosengren, N.M., Beresford, S.W., Grguric, B.A., Cas, R.A.F., 2005. An intrusive origin for the
1477 komatiitic dunite-hosted Mount Keith disseminated nickel sulfide deposit, Western Australia.
1478 *Economic Geology* 100, 149–156.
- 1479
- 1480 Søndergaard, J., Schiedek, D., Asmund, G., 2009. Environmental monitoring at the Seqi olivine
1481 mine 2008-2009. National Environmental Research Institute, Aarhus University, 42 pp.
- 1482
- 1483 Spandler, C., Mavrogenes, J., Arculus, R., 2005. Origin of chromitites in layered intrusions:
1484 Evidence from chromite-hosted melt inclusions from the Stillwater Complex. *Geology* 33, 893–
1485 896.
- 1486
- 1487 Streckeisen, A., 1973. Plutonic rocks: Classification and nomenclature recommended by the IUGS
1488 Subcommittee on the Systematics of Igneous Rocks. *Geotimes* 18, 26–30.
- 1489
- 1490 Streckeisen, A., 1976. To each plutonic rock its proper name. *Earth-Science Reviews* 12, 1–33.
- 1491
- 1492 Szilas, K., van Hinsberg, V.J., Kisters, A.F.M., Kokfelt, T.F., Scherstén, A., Windley, B.F., 2011.
1493 Remnants of Mesoarchaean oceanic crust in the Tartoq Group, South-West Greenland. *Geological*

1494 Survey of Denmark and Greenland Bulletin 23, 57–60.

1495

1496 Szilas, K., Næraa, T., Scherstén, A., Stendal, H., Frei, R., van Hinsberg, V.J., Kokfelt, T.F., Rosing,
1497 M.T., 2012a. Origin of Mesoarchaeoan arc-related rocks with boninite/komatiite affinities from
1498 southern West Greenland. *Lithos* 144, 24–39.

1499

1500 Szilas, K., Hoffmann, J.E., Scherstén, A., Rosing, M.T., Windley, B.F., Kokfelt, T.F., Keulen, N,
1501 van Hinsberg, V.J., Næraaa, T., Frei, R., Münker, C., 2012b. Complex calc-alkaline volcanism
1502 recorded in Mesoarchaeoan supracrustal belts north of Frederikshåb Isblink, southern West
1503 Greenland: Implications for subduction zone processes in the early Earth. *Precambrian Research*
1504 208, 90–123.

1505

1506 Szilas, K., Hoffmann, J., Scherstén, A., Kokfelt, T.F., Münker, C., 2013a. Archaean andesite
1507 petrogenesis: Insights from the Grædefjord Supracrustal Belt, southern West Greenland.
1508 *Precambrian Research* 236, 1–15.

1509

1510 Szilas, K., van Hinsberg, V.J., Kisters, A.F.M., Hoffmann, E., Kokfelt, T.F., Scherstén, A.,
1511 Windley, B.F., Münker, C., 2013b. Remnants of arc-related Mesoarchaeoan oceanic crust in the
1512 Tartoq Group, SW Greenland. *Gondwana Research* 23, 436–451.

1513

1514 Szilas, K., Hoffmann, J.E., Münker, C., Dzigel, A., Rosing, M.T., 2014a. Eoarchean within-plate
1515 basalts from southwest Greenland: Comment. *Geology* 42, e330–e330.

1516

1517 Szilas, K., van Gool, J.A.M., Scherstén, A., Frei, R., 2014b. The Mesoarchaeoan Storø Supracrustal
1518 Belt, Nuuk region, southern West Greenland: An arc-related basin with continent-derived
1519 sedimentation. *Precambrian Research* 247, 208–222.

1520

1521 Szilas, K., van Hinsberg, J., Creaser, R., Kisters, A.F.M., 2014c. The geochemical composition of
1522 serpentinites in the Mesoarchaeoan Tartoq Group, SW Greenland: Harzburgitic cumulates or melt-
1523 modified mantle? *Lithos* 198, 103–116.

1524

1525 Szilas, K., Kelemen, P.B., Rosing, M.T., 2015a. The petrogenesis of ultramafic rocks in the >3.7 Ga
1526 Isua supracrustal belt, southern West Greenland: Geochemical evidence for two distinct magmatic
1527 cumulate trends. *Gondwana Research* 28, 565–580.

1528

1529 Szilas, K., Kelemen, P. B., Bernstein, S., 2015b. Peridotite enclaves hosted by Mesoarchaeoan TTG-
1530 suite orthogneisses in the Fiskefjord region of southern West Greenland. *GeoResJ* 7, 22–34.

1531

1532 Szilas, K., Maher, K., Bird, D.K., 2016a. Aluminous gneiss derived by weathering of basaltic
1533 source rocks in the Neoarchean Storø Supracrustal Belt, southern West Greenland. *Chemical*
1534 *Geology* 441, 63–80.

1535

1536 Szilas, K., Tusch, J., Hoffmann, J.E., Garde, A.A., Münker, C., 2017. Hafnium isotope constraints
1537 on the origin of Mesoarchaeoan andesites in southern West Greenland, North Atlantic craton. In:
1538 Halla, J., Whitehouse, M. J., Ahmad, T. & Bagai, Z. (eds) *Crust–Mantle Interactions and Granitoid*
1539 *Diversification: Insights from Archaean Cratons*. Geological Society, London, Special Publications

- 1540 449, 19–38. <http://dx.doi.org/10.1144/SP449.2>
- 1541 Szilas, K., van Hinsberg, V.J., McDonald, I., Morishita, T., Pearson, D.G., 2016b. Highly depleted
1542 peridotites within Mesoarchaean orthogneiss at the Seqi Olivine Mine, SW Greenland - Potential
1543 implications for the formation of cratonic keels. Goldschmidt Conference, Abstract 3009,
1544 Yokohama. <http://goldschmidt.info/2016/uploads/abstracts/finalPDFs/3009.pdf>
- 1545 Terentiev, R. A., Savko, K. A., Santosh, M., 2016. Paleoproterozoic crustal evolution in the East
1546 Sarmatian Orogen: Petrology, geochemistry, Sr–Nd isotopes and zircon U–Pb geochronology of
1547 andesites from the Voronezh massif, Western Russia. *Lithos* 246, 61–80.
- 1548
- 1549 Thakurta, J., Ripley, E.M., Li, C., 2008. Geochemical constraints on the origin of sulfide
1550 mineralization in the Duke Island Complex, southeastern Alaska. *Geochemistry Geophysics*
1551 *Geosystems* 9, Q07003.
- 1552
- 1553 Tiepolo, M., Oberti, R., Zanetti, A., Vannucci, R., Foley, S.F., 2007. Trace-element partitioning
1554 between amphibole and silicate melt. *Reviews in mineralogy and geochemistry* 67, 417–452.
- 1555
- 1556 Wager, L.R., Brown, G.M., Wadsworth, W.J. 1960. Types of igneous cumulates. *Journal of*
1557 *Petrology* 1, 73–85.
- 1558
- 1559 Wan, Z., Coogan, L.A., Canil, D., 2008. Experimental calibration of aluminum partitioning between
1560 olivine and spinel as a geothermometer. *American Mineralogist* 93, 1142–1147.
- 1561
- 1562 Wang, H., van Hunen, J., Pearson, D.G., 2016. Making Archean cratonic roots by lateral

- 1563 compression: a two-stage thickening and stabilization model. *Tectonophysics* (**in press**).
- 1564
- 1565 Warren, J.M., 2016. Global Variations in Abyssal Peridotite Compositions. *Lithos* 248–251, 193–
- 1566 219.
- 1567
- 1568 Witt-Eickschen, G., Seck, H.A., 1991. Solubility of Ca and Al in orthopyroxene from spinel
- 1569 peridotite: an improved version of an empirical geothermometer. *Contributions to Mineralogy and*
- 1570 *Petrology* 106, 431–439.
- 1571
- 1572 Wittig, N., Pearson, D.G., Webb, M., Ottley, C.J., Irvine, G.J., Kopylova, M., Jensen, S.M., Nowell
- 1573 G.M., 2008. Origin of cratonic lithospheric mantle roots: a geochemical study of peridotites from
- 1574 the North Atlantic Craton, West Greenland. *Earth and Planetary Science Letters* 274, 24–33.
- 1575
- 1576 Wittig, N., Pearson, D.G., Baker, J.A., Duggen, S., Hoernle, K., 2010. A major element, PGE and
- 1577 Re–Os isotope study of Middle Atlas (Morocco) peridotite xenoliths: evidence for coupled
- 1578 introduction of metasomatic sulphides and clinopyroxene. *Lithos* 115, 15–26.
- 1579
- 1580 Wooden, J.L., Czamanske, G.K., Zientek, M.L., 1991. A lead isotopic study of the Stillwater
- 1581 Complex, Montana: constraints on crustal contamination and source regions. *Contributions to*
- 1582 *Mineralogy and Petrology* 107, 80–93.
- 1583
- 1584 WSU, 2016. Washington State University GeoAnalytical Lab. Technical notes describing sample
- 1585 preparation, analytical procedure, precision, and accuracy of XRF and ICP-MS analysis can be

1586 found at this link: <http://environment.wsu.edu/facilities/geolab/technotes>

1587

1588 Zhao, G., Wilde, S.A., Li, S., Sun, M., Grant, M.L., Li, X., 2007. U–Pb zircon age constraints on
1589 the Dongwanzi ultramafic–mafic body, North China, confirm it is not an Archean ophiolite. *Earth
1590 and Planetary Science Letters* 255, 85–93.

1591

1592 Zientek, M.L., 2012. Magmatic ore deposits in layered intrusions-Descriptive model for reef-type
1593 PGE and contact-type Cu-Ni-PGE deposits (No. 2012–1010). US Geological Survey.

1594

1595 **Figure captions**

1596

1597 **Figure 1.** Simplified geological map of the Nuuk region with the Seqi Ultramafic Complex and
1598 several similar complexes along Fiskefjord marked in bold. The red square outlines the area of the
1599 detailed map of the Seqi Ultramafic Complex shown in **Fig. 2**. Red circle marks Nuuk, the capital
1600 of Greenland. The regional supracrustal belts range in age from Eo- to Neoproterozoic. Regional
1601 mapping based on fieldwork by the Geological Survey of Denmark and Greenland (GEUS).

1602

1603 **Figure 2.** Detailed map of the Seqi Ultramafic Complex modified from Dahl (2004). The four main
1604 lithological units are shown, whereas chromitite bands and amphibolite veins are too small to
1605 outline at this scale and their presence is only marked by the sample positions. Note that we use
1606 peridotite (*sensu lato: s.l.*) in the broadest sense, and include all olivine-dominated (>40% modal
1607 olivine) plutonic rocks that are not strictly dunite (>90% modal olivine) c.f. Streckeisen (1976). The
1608 Seqi peridotites (*s.l.*) thus include various modal combinations of olivine–orthopyroxene–

1609 amphibole that do not outline any mapable systematics, but rather reflect mixtures of these
1610 minerals, which are mostly classified as amphibole–harzburgites. The Seqi Ultramafic Complex
1611 appears fragmented and its inclusion within the hosting tonalitic gneiss demonstrates that the latter
1612 was intrusive and thus postdates the formation of the ultramafic rocks. The outline of the open pit of
1613 the Seqi Olivine Mine in the western body of the Seqi Ultramafic Complex is marked with a
1614 stippled grey line.

1615

1616 **Figure 3.** Field observations from the Seqi Ultramafic Complex. (a) Overview of the open pit of the
1617 Seqi Olivine Mine exposing walls of homogeneous dunite, which was the main ore during the
1618 operation of the mine. (b) Porphyritic dunite with showing euhedral olivine crystals up to about 2
1619 cm long. (c) Peridotite with minor amounts of amphibole present interstitially. (d) Chromitite
1620 forming cm-thick stratiform layers in orthopyroxene-rich peridotite. (e) Layered dunite showing
1621 small ridges on the weathered surface where the modal content of chromite is elevated. (f) Poikilitic
1622 peridotite with round orthopyroxene oikocrysts up to 5 cm across. (g) Peridotite with green
1623 amphibole (tremolite) in coarse dunite ± orthopyroxene. Note the brecciated nature of the dunite
1624 within the amphibole domain (finger for scale). (h) Intrusive tonalitic sheet (sample 186451)
1625 showing strong reaction with the hosting homogeneous dunite. Zircon from this rock was dated at
1626 2963 ± 6 Ma by LA-ICP-MS (see **Section 5.5**). (i) Amphibole and talc veins cut apparent layering
1627 in porphyritic dunite. Note the coarse grain size of the upper dunite unit in comparison with the
1628 lower. (j) Tightly folded chromitite layer in the NE part of the Seqi Ultramafic Complex. The head
1629 of the hammer that is used for scale in the above photographs is about 20 cm wide. Additional field
1630 photographs are presented in **Appendix A**.

1631

1632 **Figure 4.** Representative polarized light microscopy photographs of the various lithological units
1633 found in the Seqi Ultramafic Complex. Each set shows plane polarized light (PPL) on the left and
1634 crossed polarized light (XPL) on the right. The scale bar in each lower right corner represents 1000
1635 μm (1 mm) in all frames. The following mineral abbreviations are used: amphibole (Am), olivine
1636 (Ol), orthopyroxene (Opx), phlogopite (Phl) and spinel (Spl). See **Section 3** for a detailed
1637 petrographic description of the each of the rock types. Additional microscope photographs are
1638 presented in **Appendix B**.

1639

1640 **Figure 5.** Back scattered electron (BSE) images (by EMPA) of the various rock units found in the
1641 Seqi Ultramafic Complex. Note that the first four horizontal panels are each for a single rock type,
1642 whereas the lower panel is for three different rock types. The following mineral abbreviations are
1643 used: amphibole (Am), chlorite (Chl), ilmenite (Ilm), olivine (Ol), orthopyroxene (Opx), phlogopite
1644 (Phl), spinel (Spl) and talc (Tlc). Additional BSE images are presented in **Appendix C**.

1645

1646 **Figure 6.** Back-scattered electron (BSE) images (by SEM) of representative zircon grains showing
1647 magmatic textures with internal zoning. Spot positions are marked together with their $^{207}\text{Pb}/^{206}\text{Pb}$
1648 age (2σ error) and their concordance is indicated in parenthesis. The sample positions are indicated
1649 on the map in **Fig. 2**. (a) Sample 186456 is part of the regional orthogneiss that fragmented the Seqi
1650 Ultramafic Complex. (b) Sample 186451 is from an intrusive tonalitic (**Fig. 3h**) in the
1651 homogeneous dunite, which has a significant reaction rim consisting of mainly chlorite and
1652 amphibole. (c) Sample 186453 is from a NE–SW trending granitoid pegmatite (**Fig. A5** in
1653 Appendix A).

1654

1655 **Figure 7.** Bulk-rock major element compositions of the Seqi rocks (this study) plotted in
1656 comparison with regional data for regional ultramafic (MgO >20 wt.%) enclaves in the
1657 Mesoarchaeon Akia terrane marked in grey shade (Akia data from: Garde, 1997; Kristensen, 2006;
1658 Szilas et al., 2015b). A similar comparison for trace elements is presented in **Appendix D (Fig.**
1659 **D1)**. All of the new bulk-rock data for the Seqi rocks are available in the supplementary **Table S1**.

1660

1661 **Figure 8.** Bulk-rock trace element diagrams for the Seqi rocks normalised to primitive mantle
1662 (Palme and O'Neill, 2003). The shaded area outlines the total range of the data for comparison.
1663 Note the consistent positive Pb–Hf–Zr anomalies and the elevated Th–U–La relative to Nb, which
1664 may indicate some degree of contamination with continental crust. The negative Sr–Eu anomalies
1665 suggest fractionation in equilibrium with plagioclase from the parental magma, whereas the positive
1666 Ti reflects the addition of cumulus chromite. All of the new bulk-rock data for the Seqi rocks are
1667 available in the supplementary **Table S1**.

1668

1669 **Figure 9.** Bulk-rock siderophile element diagrams for the Seqi rocks normalised to primitive mantle
1670 (PM) of Becker et al. (2006). Note that most of the Seqi samples have elevated Os and Ir
1671 abundances relative to primitive mantle, and that their normalised patterns are generally negative
1672 with a distinct positive Au-anomaly. Four samples have troughs at Os and Ir, indicating early
1673 saturation of IPGE-alloys in these particular samples. There is a general positive correlation
1674 between IPGE abundances and chromite contents for the Seqi Ultramafic Complex (see **Appendix**
1675 **D)**. The bulk-rock siderophile element data are available in the supplementary **Table S2**.

1676

1677 **Figure 10.** Olivine forsterite contents (Mg#) of the different rock units of the Seqi Ultramafic

1678 Complex (electron microprobe data). The median (thick lines) lies in a box that comprises 50% of
1679 the data (inter-quartile range; IQR) and the 'whiskers' extend to 1.5 times IQR on either side. Note
1680 that the layered dunite and the homogeneous dunite display a bimodal distribution, which is
1681 correlated with the bulk-rock mg# contents of these particular samples (see **Fig. 11a**). Note that
1682 these two rock types also show some scatter to higher forsterite compositions at rims in contact with
1683 spinel. Also note that in this work we distinguish between bulk-rock 'mg#' (which uses ΣFe) and
1684 mineral 'Mg#' (which uses Fe^{2+}). All of the electron microprobe data for the Seqi Ultramafic
1685 Complex are available in the supplementary **Table S3**.

1686

1687 **Figure 11.** (a) Forsterite contents versus bulk-rock mg# for the Seqi rocks, showing a consistent
1688 olivine composition regardless of the bulk-rock composition (horizontal trends). This suggests that
1689 the olivine compositions reflect the primary Mg/Fe ratio of the melt at the time it crystallized, and
1690 that the bulk-rock compositions are the result of accumulation of Fe-rich cumulus chromite. (b) Part
1691 of a pyroxene ternary diagram with the endmembers of wollastonite (Wo), enstatite (En) and
1692 ferrosilite (Fs), showing the composition of the measured Seqi amphibole converted to
1693 corresponding anhydrous clinopyroxene compositions, as well as the measured orthopyroxene
1694 compositions. Note that if this augite composition is representative of the igneous conditions, it
1695 would point to temperatures of above 1300°C according to the experimental work of Lindsley
1696 (1983) and Lindsley and Andersen (1983). NB. Clinopyroxene has not been directly observed in
1697 any of the studied rocks from the Seqi Ultramafic Complex, although we expect this mineral to
1698 have been a primary igneous phase (see **Section 5.3**).

1699

1700 **Figure 12.** Spinel compositions from the Seqi Ultramafic Complex. The fields of abyssal

1701 harzburgite (residual mantle) and dunite (melt channels) are from Warren (2016) and the field of
1702 Oman chromitite is from Rollinson (2005). The spinel compositions clearly demonstrate that the
1703 Seqi Ultramafic Complex does not represent a mantle fragment. The electron microprobe mineral
1704 data for the Seqi Ultramafic Complex are available in the supplementary **Table S3**.

1705

1706 **Figure 13.** LA-ICP-MS trace element data for individual minerals from the Seqi Ultramafic
1707 Complex normalised to primitive mantle of Palme and O'Neill (2003). Note that amphibole has the
1708 highest abundance of incompatible trace elements of the measured minerals, and that it displays
1709 negative anomalies for Ta–Nb–Ti, which may indicate it originally formed as igneous
1710 clinopyroxene, rather than representing igneous amphibole. Also, note that spinel is enriched in Ti
1711 (and Ta), and thus could impose negative anomalies for these particular elements on the magma
1712 from which it crystallized, which is indeed observed in tholeiitic metabasalts of this region (e.g.,
1713 Garde, 2007; Polat et al., 2011; Szilas et al. 2014b). The grey area marks the total range of the Seqi
1714 mineral data. The LA-ICP-MS data for the Seqi Ultramafic Complex are available in the
1715 supplementary **Table S4**.

1716

1717 **Figure 14.** Tera-Wasserburg concordia diagrams for the three intrusive granitoid rocks at the Seqi
1718 Ultramafic Complex. The red curve at the right side of each diagram displays the cumulative
1719 distribution of the $^{207}\text{Pb}/^{206}\text{Pb}$ ratios and the error ellipses represent 2σ error. (a) Sample 186456
1720 (tonalitic orthogneiss) has an interpreted magmatic age of 2978 ± 8 Ma. (b) Sample 186451
1721 (tonalite sheet) has an interpreted magmatic age of 2963 ± 6 Ma. (c) Sample 186453 (pegmatite)
1722 has an interpreted magmatic age of 2940 ± 5 Ma. All of the U–Pb isotope data for the three
1723 granitoid rocks are available in the supplementary **Table S5**.

1724

1725 **Figure 15.** Examples of room temperature Mössbauer spectra of chromite in chromitite samples
1726 186483 (a) and 186469 (b) from the Seqi Ultramafic Complex. The spectra were fitted as $3\text{Fe}^{2+}(\text{A})$
1727 $+1\text{Fe}^{3+}(\text{B})$ and $\text{Fe}^{2+}(\text{A}) + \text{Fe}^{2+}(\text{B}) + \text{Fe}^{3+}(\text{B})$, respectively. The data and the remaining spectra are
1728 provided in the supplementary **Table S6**.

1729

1730 **Figure 16.** Constraints on the oxygen fugacity of the Seqi rocks given as $\text{Fe}^{3+}/\Sigma\text{Fe}$. The Fe^{3+}
1731 proportion was determined by Mössbauer spectroscopy in addition to measurements by electron
1732 microprobe and LA-ICP-MS assuming spinel stoichiometry (see **Section 5.3**). The data are plotted
1733 against temperatures calculated by Cr–Al in orthopyroxene in the same samples, and are thus only
1734 given for samples in which this mineral was present.

1735

1736 **Figure 17.** Pressure versus temperature phase diagram showing calculated pseudosections for six
1737 ultramafic rock from the Seqi Ultramafic Complex. Estimated pressure-temperature conditions for
1738 peak metamorphism of the Seqi Ultramafic Complex are 700 to 900°C at 1.0 to 2.3 GPa, as
1739 constrained from the overlap in pseudosection mineral assemblage fields for six samples ranging
1740 from dunite, to peridotite, to chromitite, to amphibolite. This field is bounded by the lack of
1741 clinopyroxene, garnet, plagioclase, talc, tremolite and serpentine at peak conditions. If
1742 clinopyroxene was present, the field expands to higher pressure and temperature (dashed field in the
1743 inset). The inset shows additional constraints from geothermobarometers applied to mineral rims
1744 and contact pairs. P88 - Ni–Mg exchange between olivine and orthopyroxene (Povdin, 1988);
1745 BK90 - Ca in orthopyroxene (Brey and Köhler, 1990); B91 - Mg–Fe exchange between olivine and
1746 spinel (Ballhaus et al., 1991); WES91 - Al in orthopyroxene (Witt-Eickschen and Seck, 1991);

1747 LG03 - Mg–Fe exchange between olivine and orthopyroxene (Liermann and Ganguly, 2008); dH10
1748 – Ca, Al and Cr in olivine (de Hoog et al., 2010). The following mineral abbreviations are used:
1749 amphibole (Am), clinopyroxene (Cpx), garnet (Grt), orthopyroxene (Opx), phlogopite (Phl),
1750 plagioclase (Plag), spinel (Spl), olivine (Ol), serpentine (Srp), talc (Tlc), and tremolite (Tr).

1751

1752 **Figure 18.** Various plots comparing the different rock types of the Seqi Ultramafic Complex with
1753 the bulk-rock compositions of cumulate derived from komatiitic melts. Note that despite the highly
1754 forsteritic composition of the Seqi Ultramafic Complex, none of these plots support a komatiitic
1755 affinity. The reference komatiite data are from Fiorentini et al. (2011).

1756

1757 **Figure 19.** Spinel compositions from all of the Seqi rocks (blue dots) plotted against spinel from
1758 three different magma types: (1) layered intrusions, (2) komatiites and (3) Alaskan-type zoned
1759 complexes (reference data are from Barnes and Roeder, 2001). As also noted in **Fig. 18**, komatiites
1760 do not have the appropriate characteristics to explain the highly forsteritic rocks of the Seqi
1761 Ultramafic Complex. The low Fe^{3+} content of the Seqi spinel is also not compatible with an arc-
1762 related origin, such as that of Alaskan-type zoned complexes (Burns, 1985; Thakurta et al., 2008).
1763 For clarity, the ranges of spinel from layered intrusions have not been plotted in the two latter
1764 diagrams where they essentially overlap with the compositions of the Seqi spinel, thus supporting
1765 an affinity of the Seqi Ultramafic Complex with other layered intrusions in general.

1766

1767 **Supplementary material**

1768

1769 Appendix A. Field observations from the Seqi Ultramafic Complex.

1770

1771 Appendix B. Polarized light microscopy photographs.

1772

1773 Appendix C. Back-scattered electron (BSE) microprobe images.

1774

1775 Appendix D. Supplementary geochemical diagrams.

1776

1777 Table S1. Bulk-rock major and trace element data from Washington State University.

1778

1779 Table S2. Bulk-rock platinum-group element data from Cardiff University.

1780

1781 Table S3. Electron microprobe mineral data from Stanford University.

1782

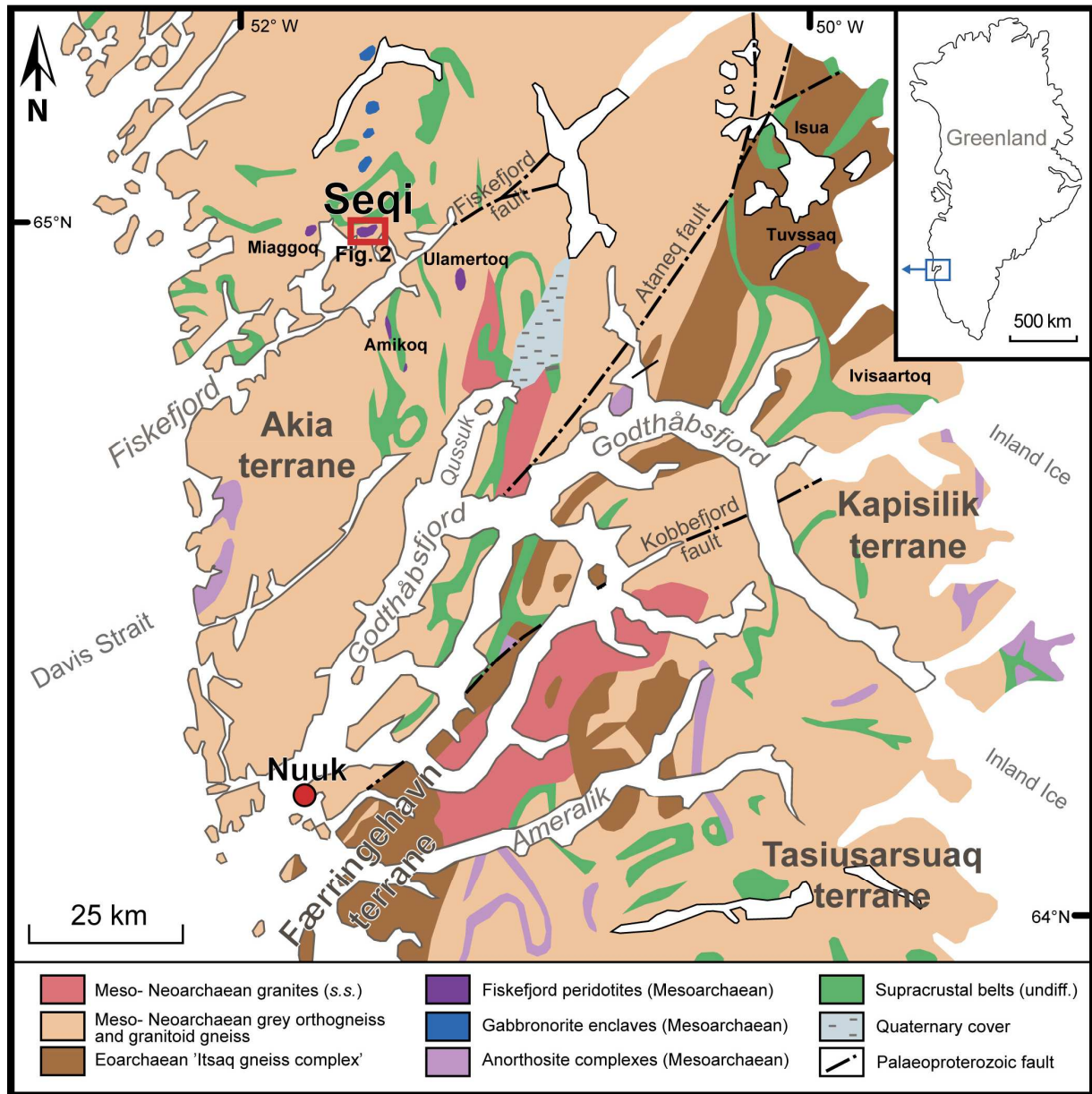
1783 Table S4. *In situ* LA-ICP-MS trace element mineral data from McGill University.

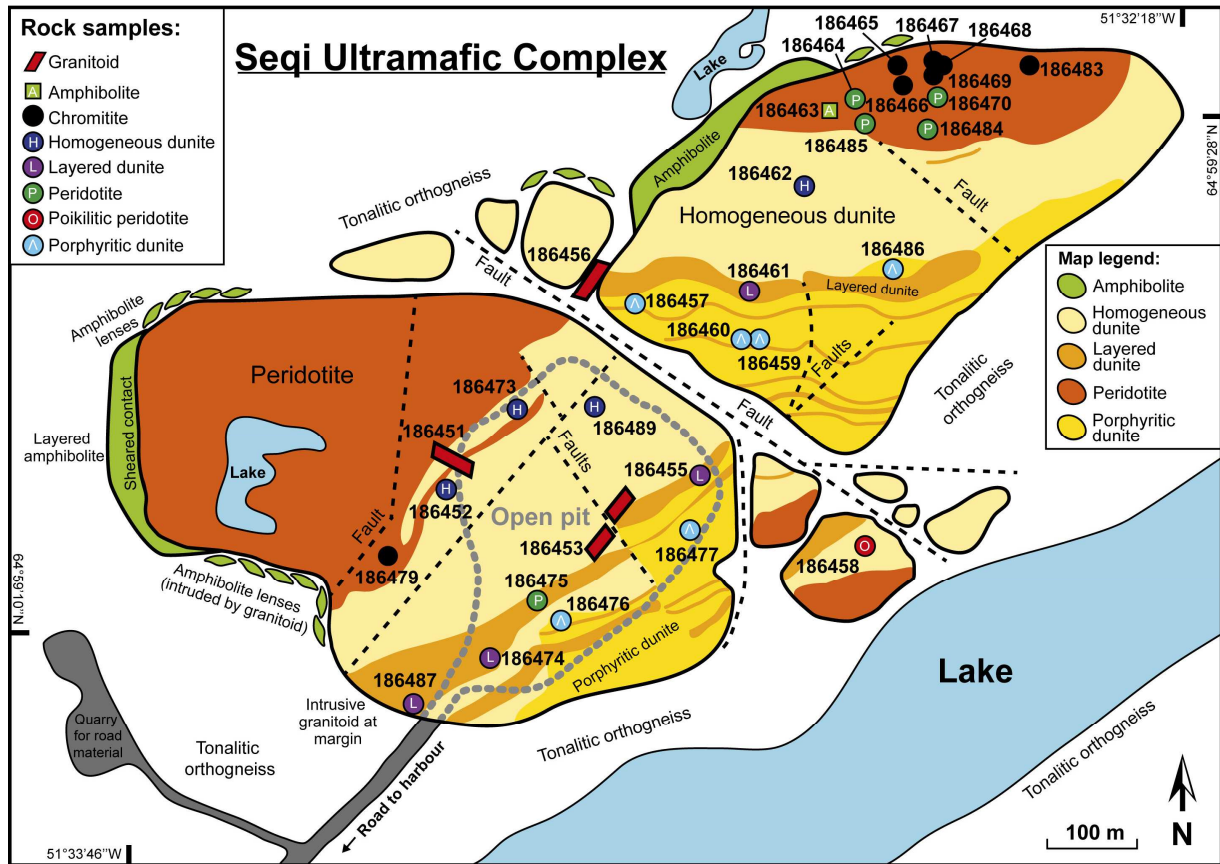
1784

1785 Table S5. *In situ* U–Pb zircon data from the Geological Survey of Denmark and Greenland.

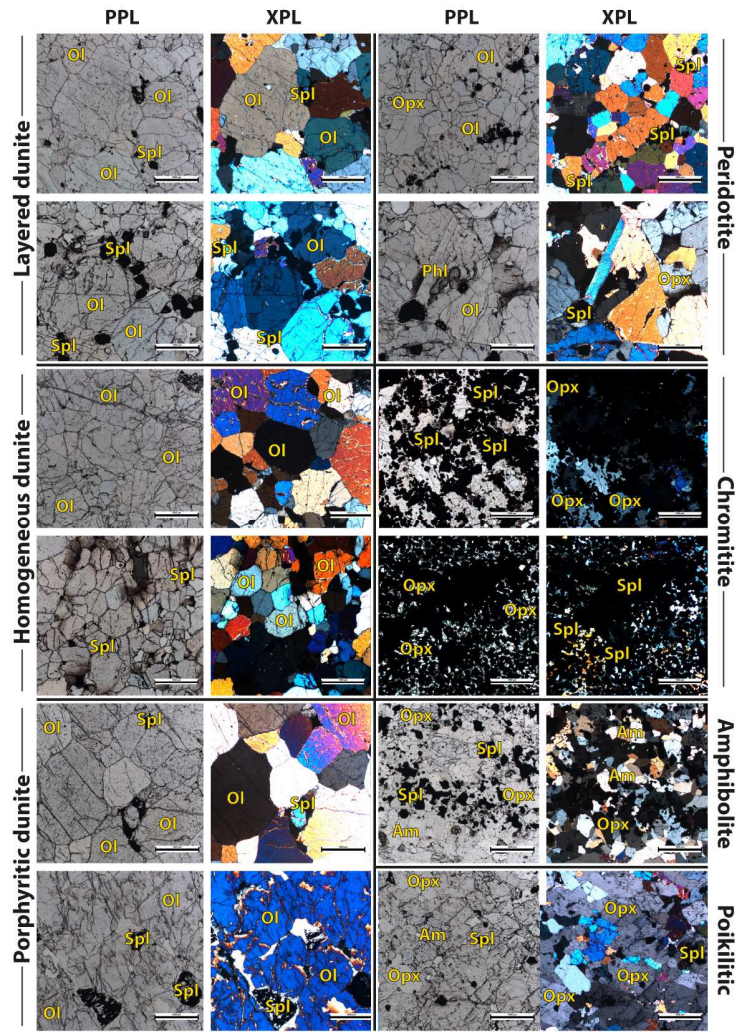
1786

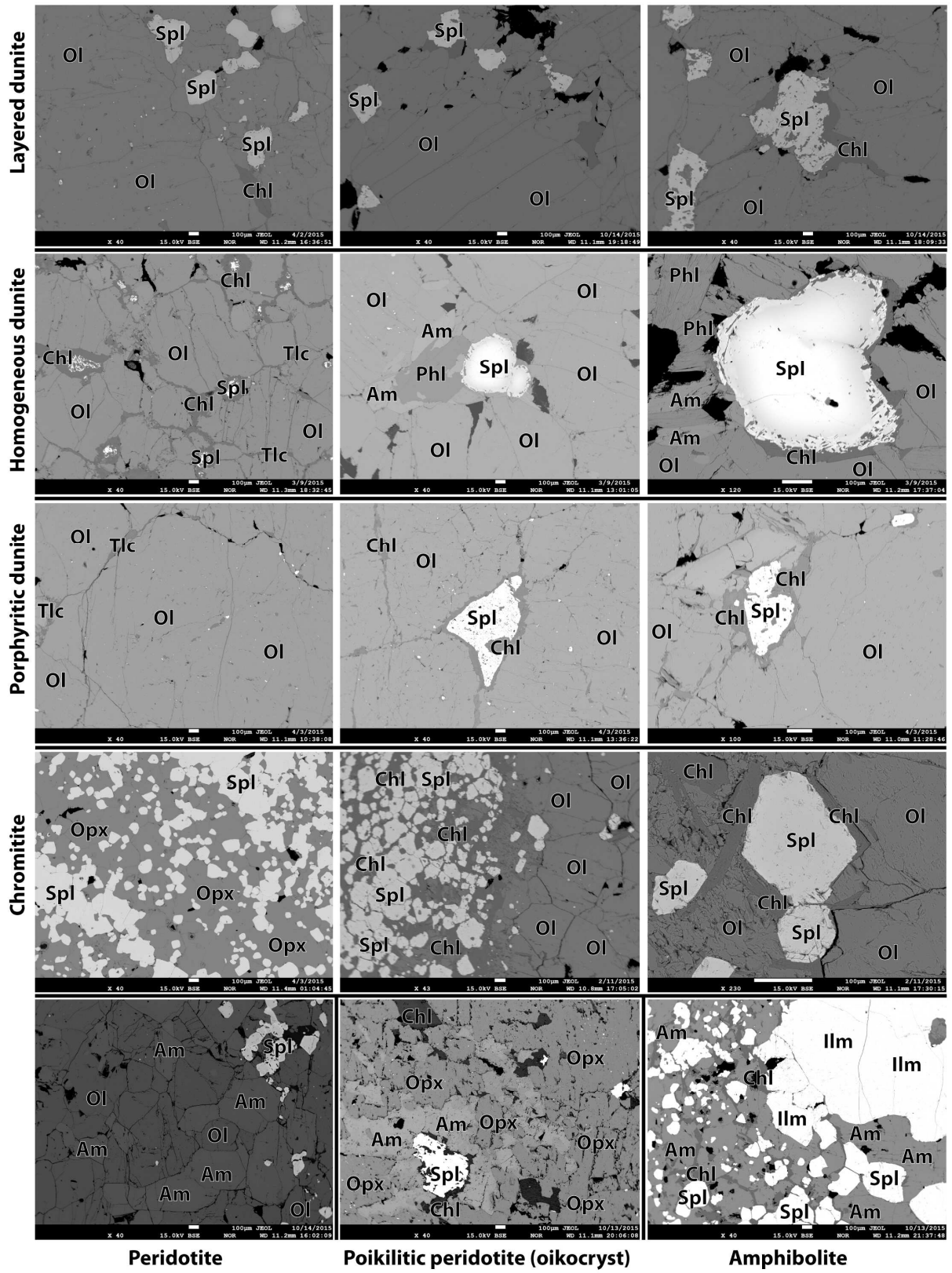
1787 Table S6. Mössbauer spectroscopy data from Derby University.

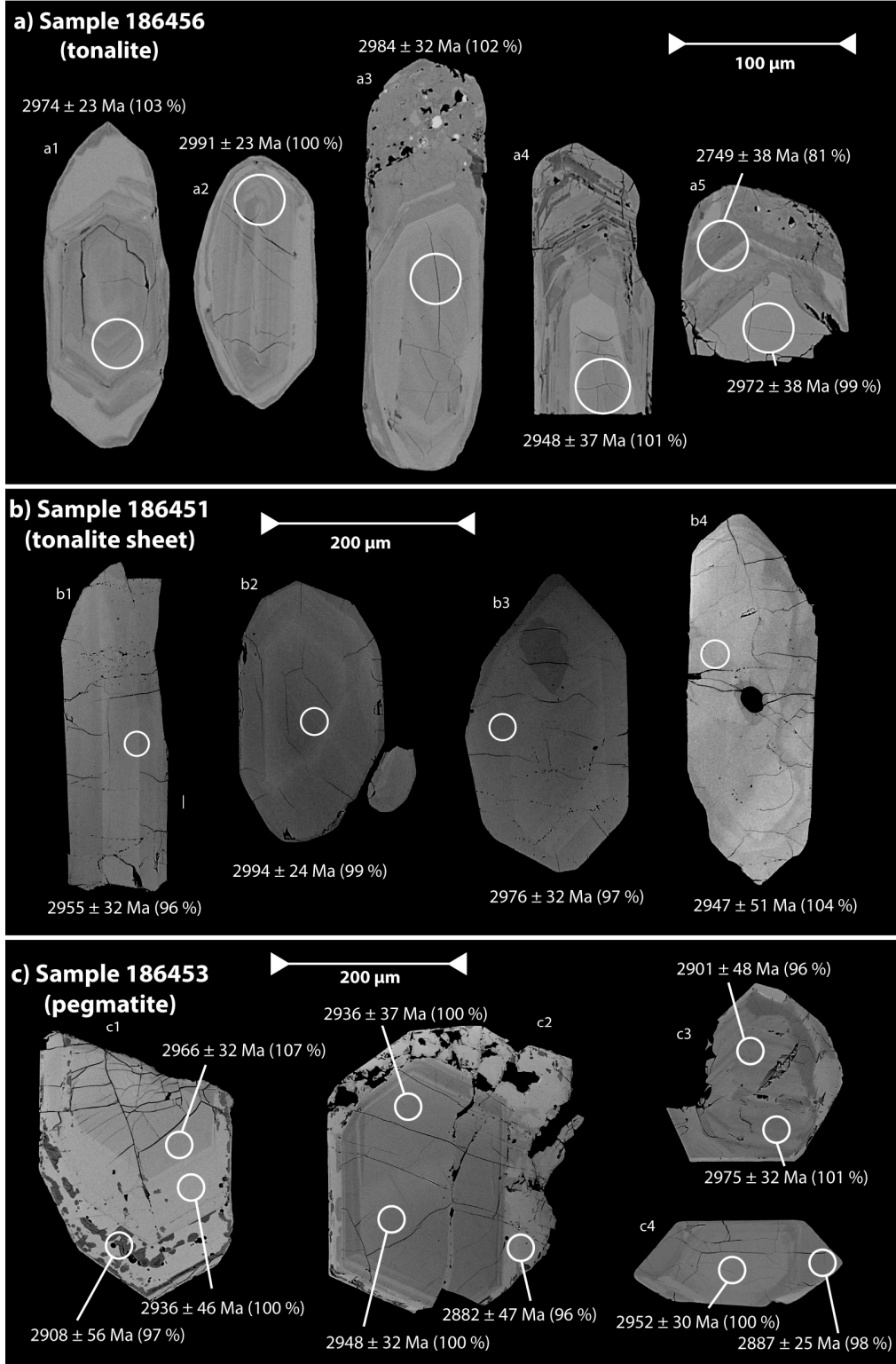


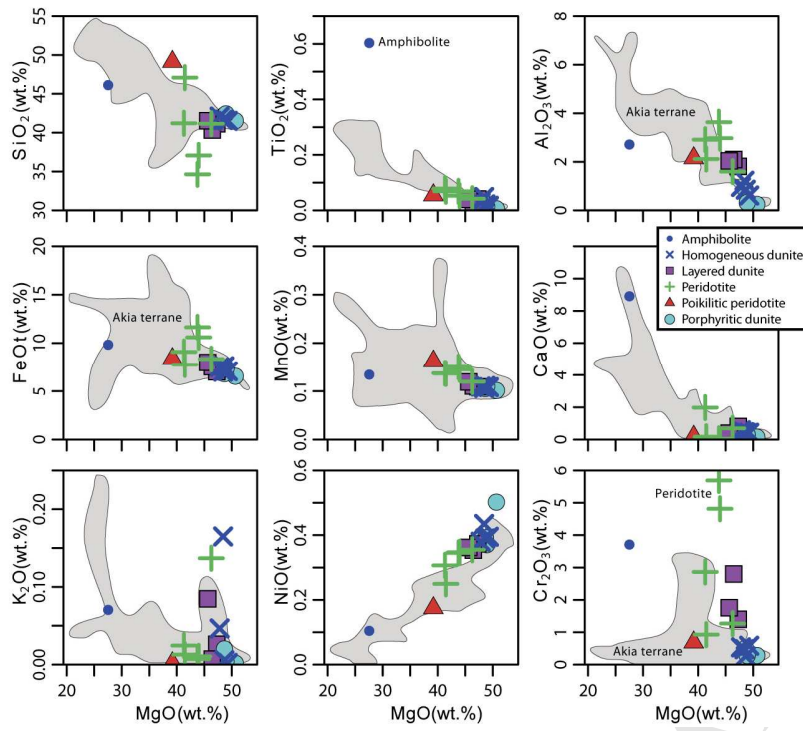


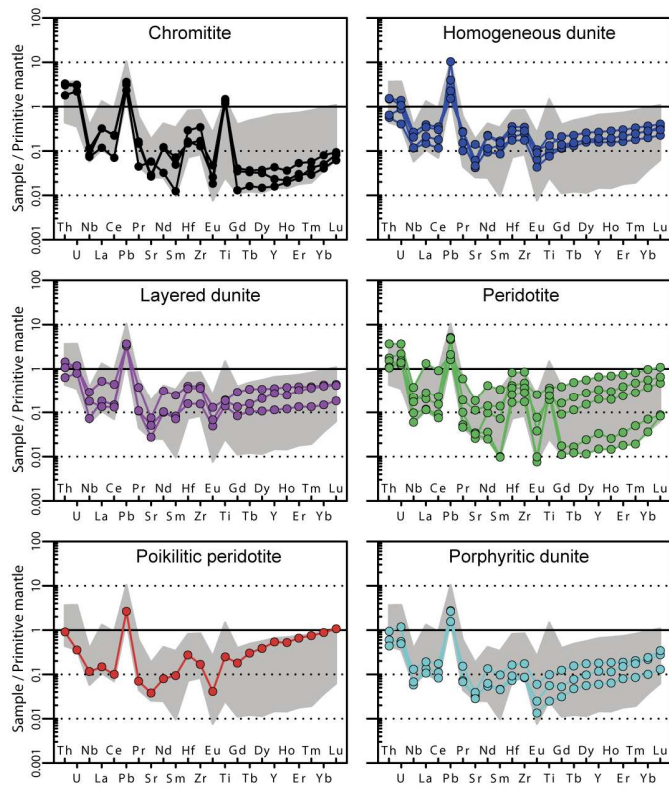


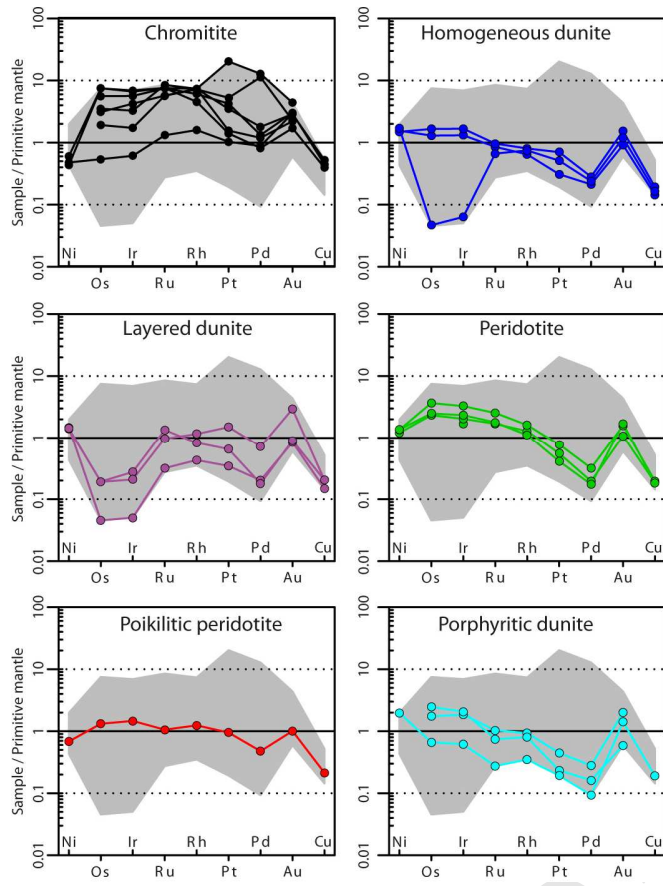


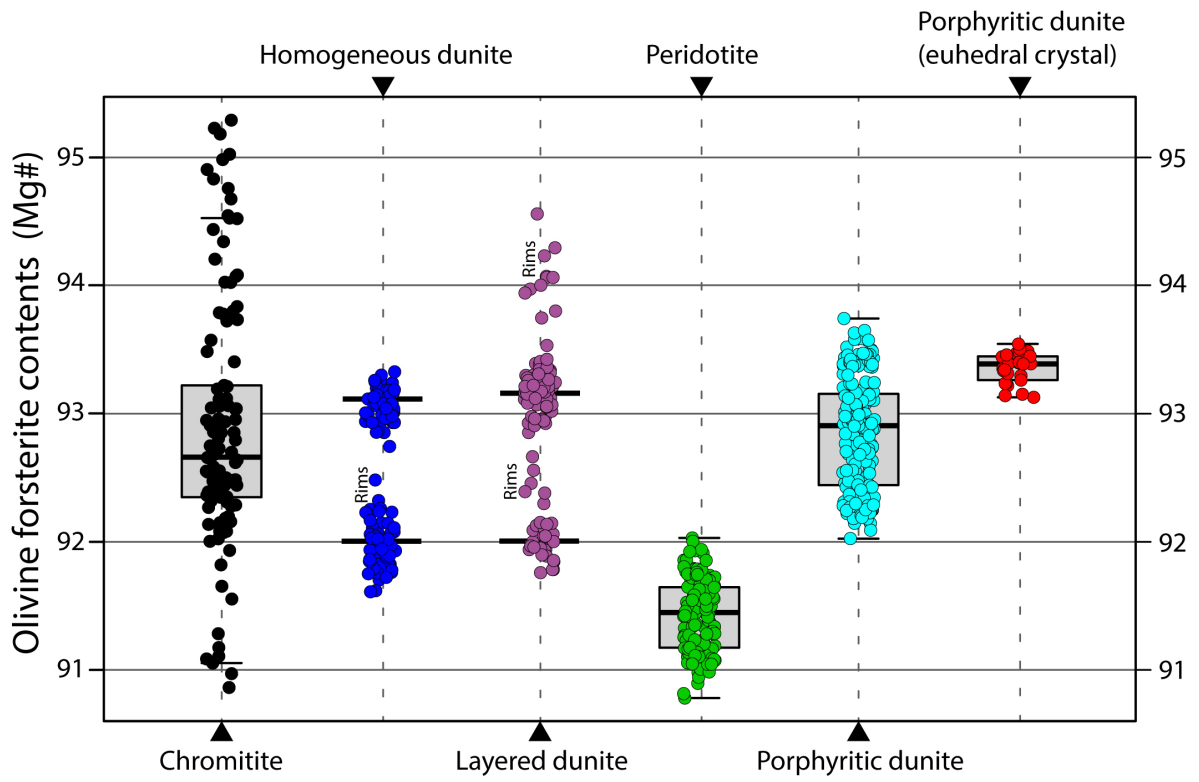


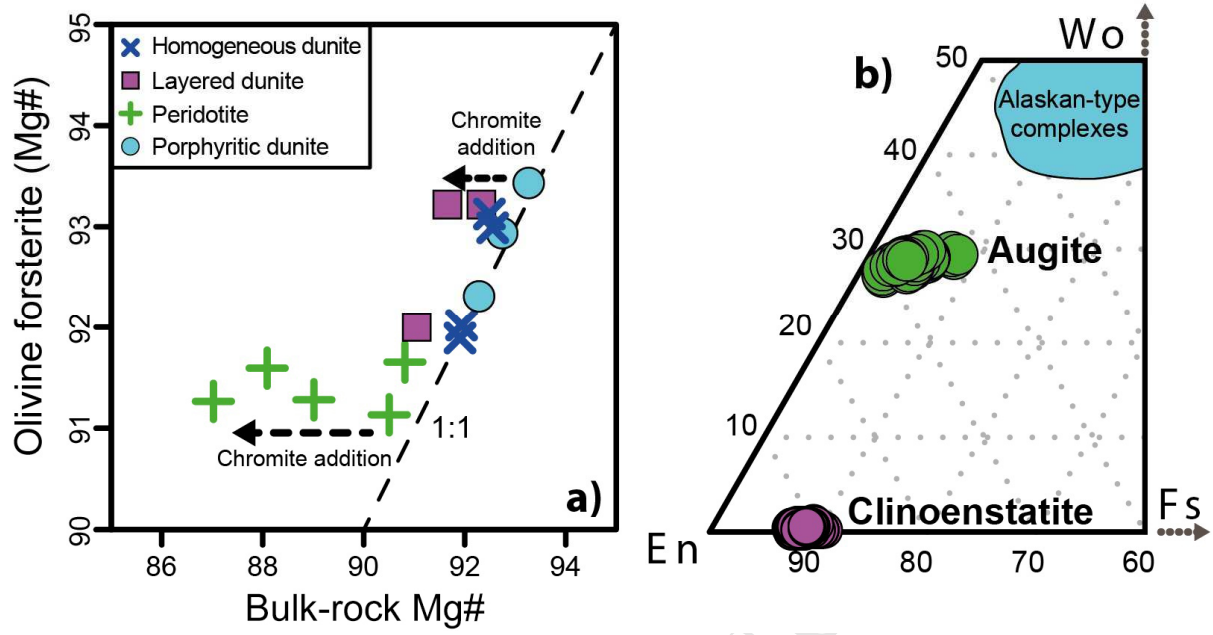


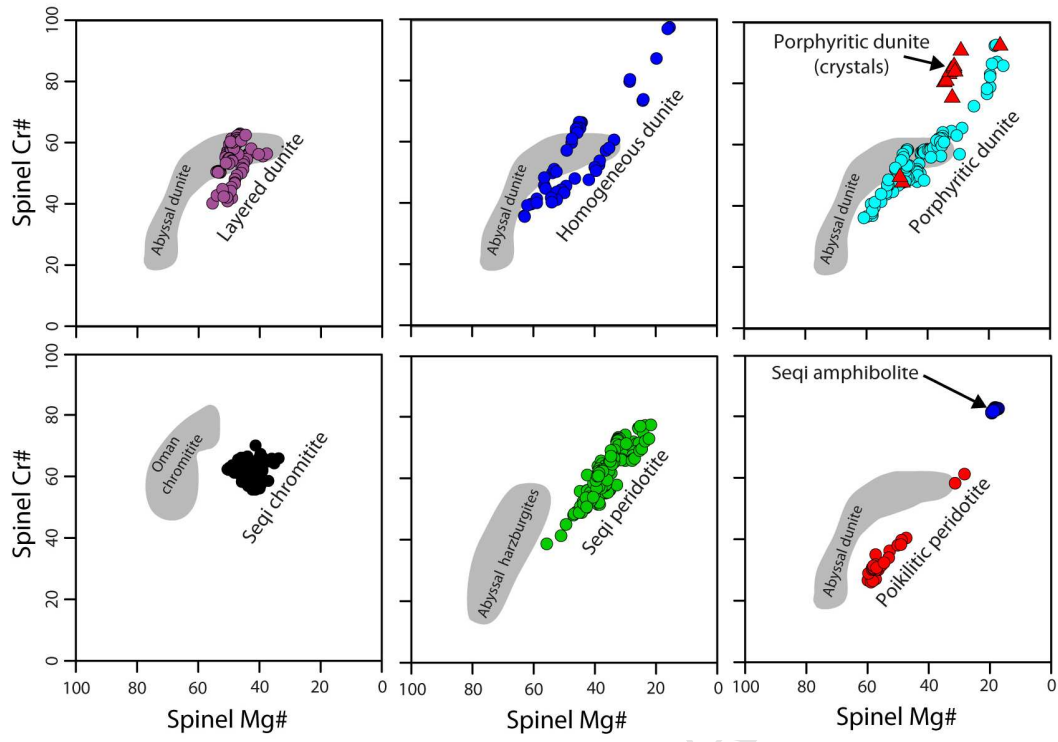


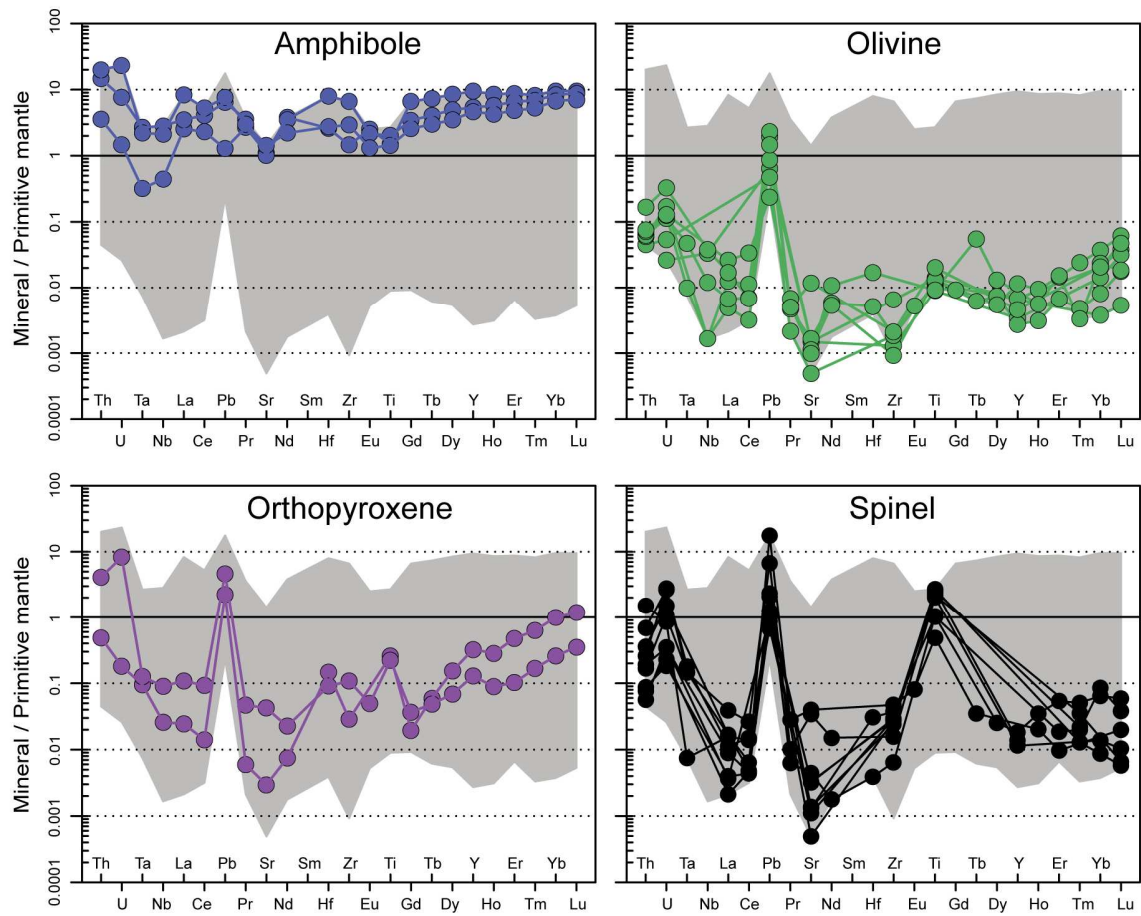




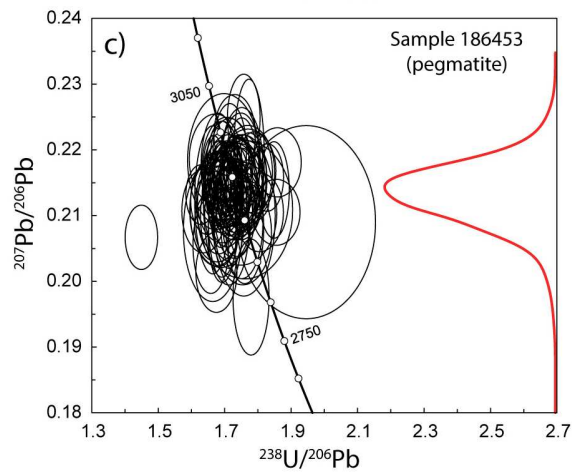
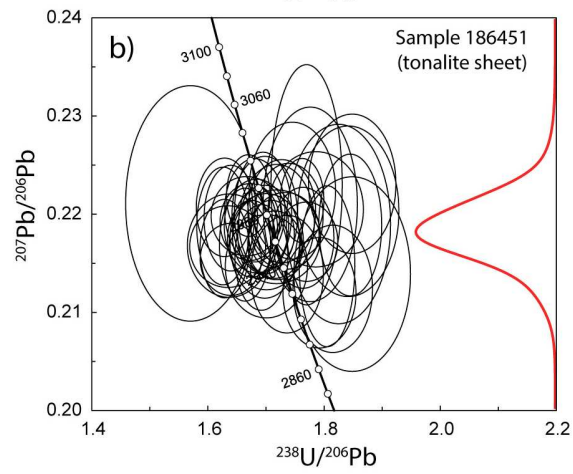
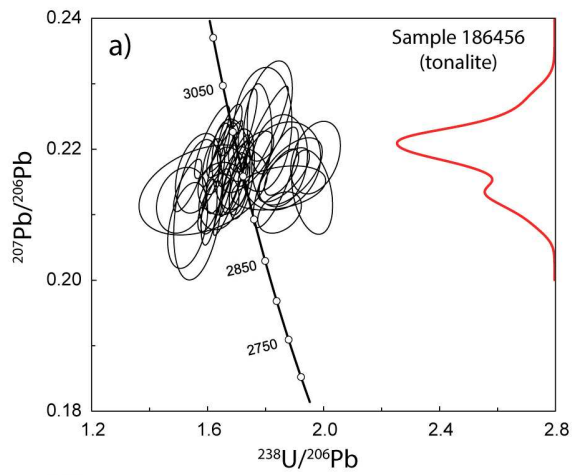


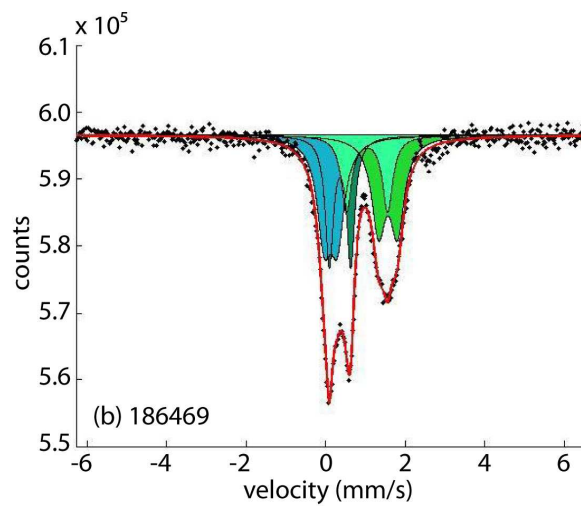
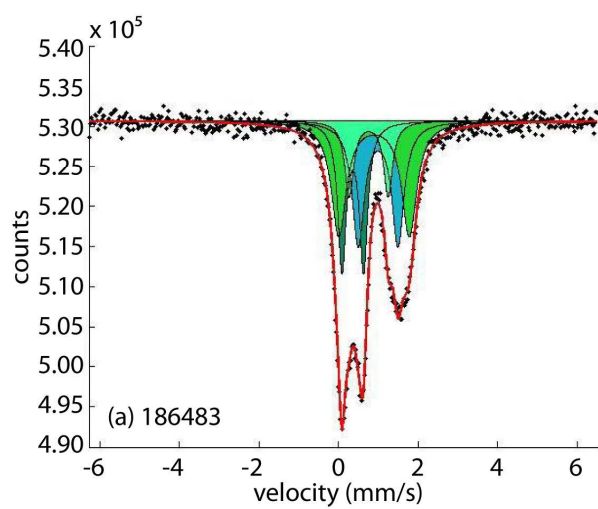




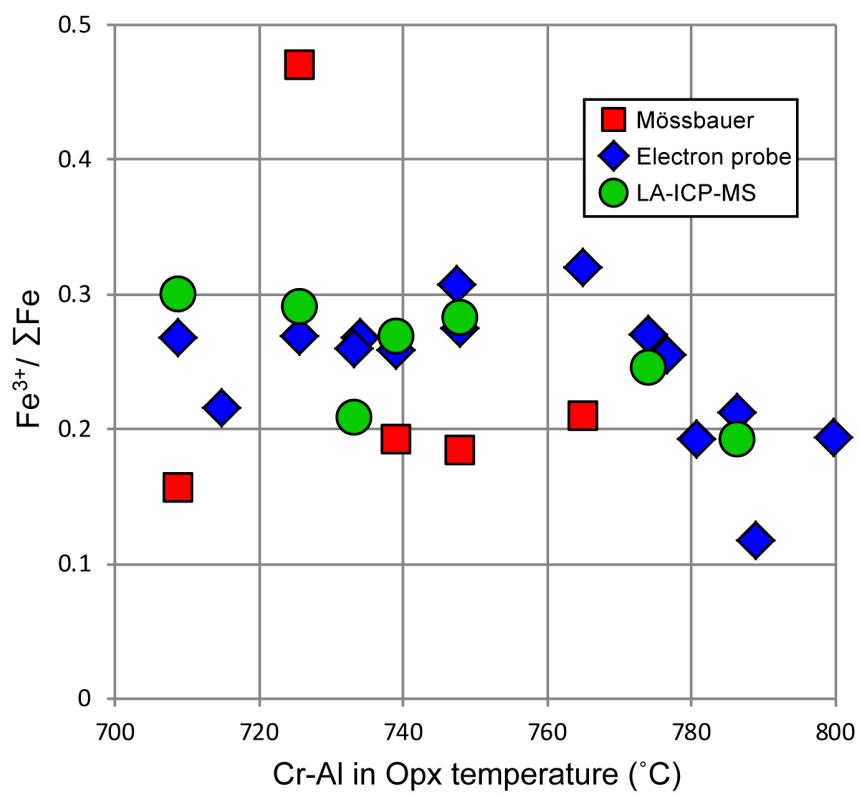


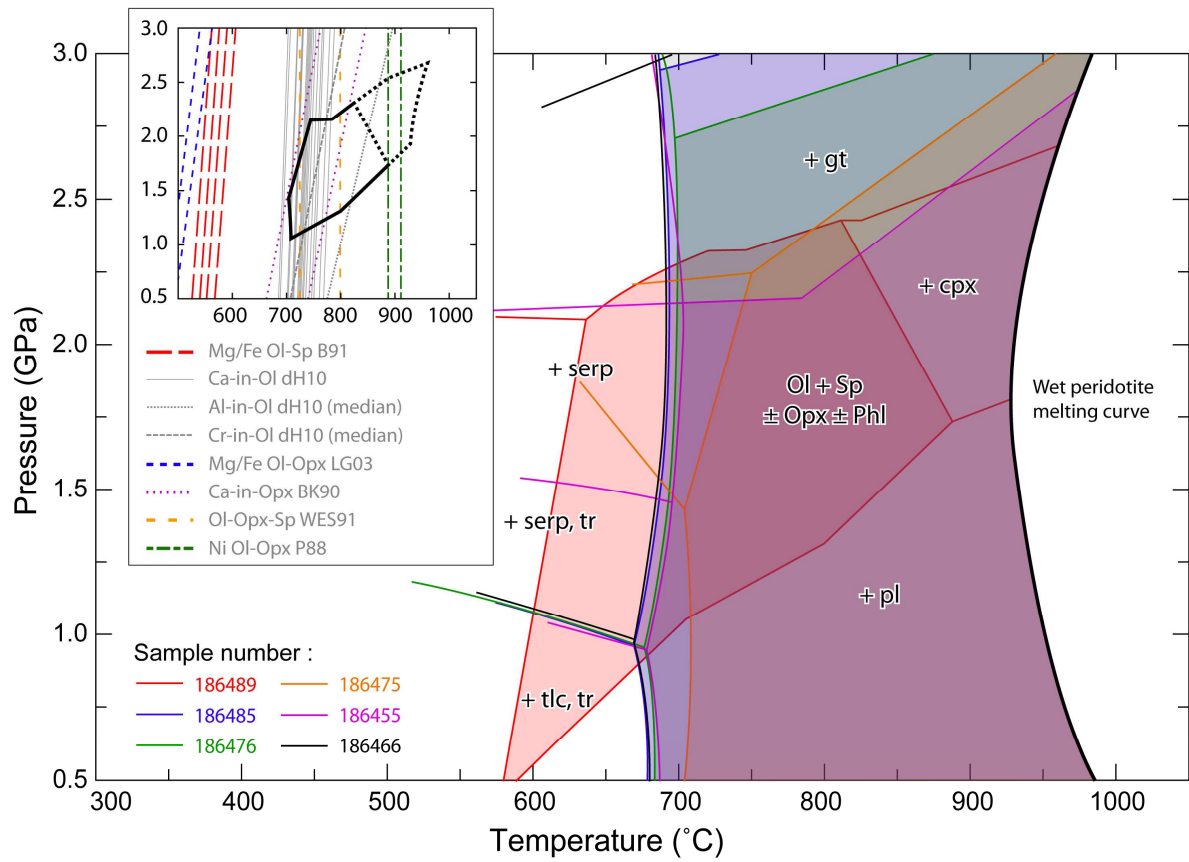
ACCEPTED

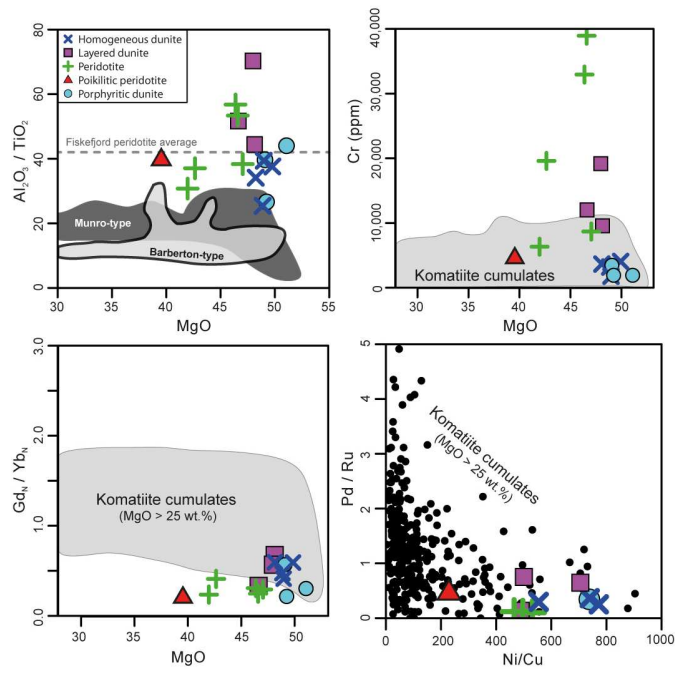


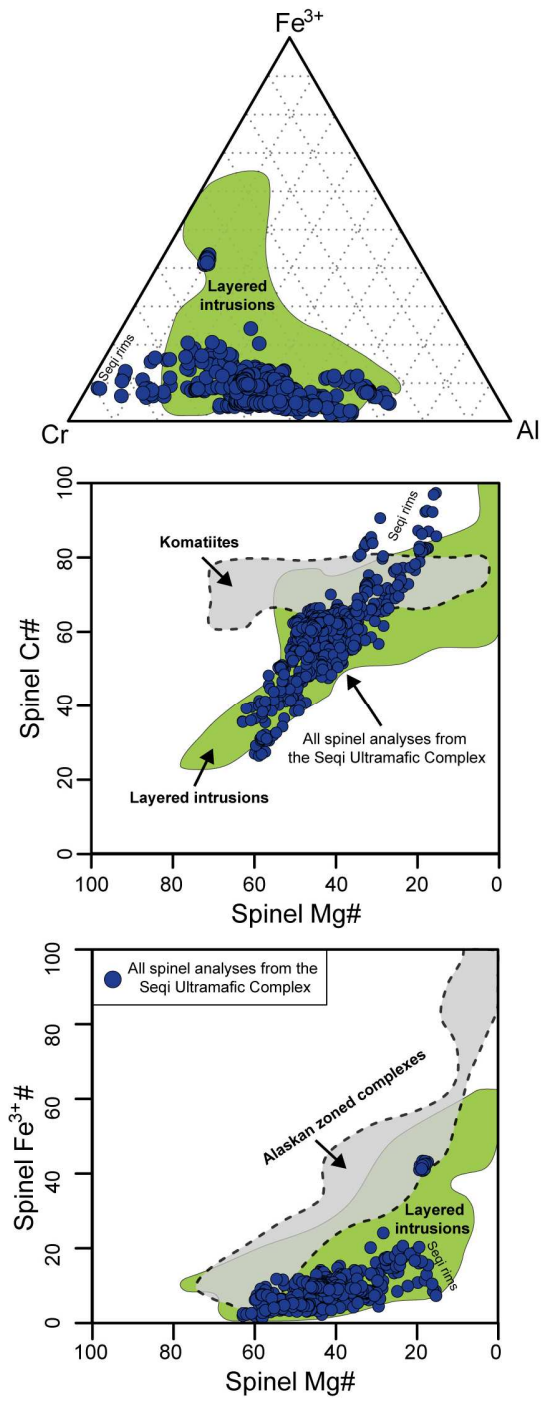


ACCEPTED MANUSCRIPT









Research highlights:

- The Seqi Ultramafic Complex is intruded by a 2978 ± 8 Ma granitoid sheet.
- Highly forsteritic olivine with Mg# ranging from around 91 to 93.
- Stratiform chromitite and layered dunite points to *in situ* cumulus crystallization.
- IPGE fractionation supports a cumulate origin for the ultramafic rocks.
- Parental magma could have been complementary to regional SCLM.